修士論文

Surface-Normal Electro-Optic Polymer Modulator using Single-Layer Plasmonic Grating

（単層プラズモニックグレーティングを用いた垂直入射型電気光学ポリマー変調器）

2024 年 7 月 22 日提出

指導教員　　中野 義昭 教授

東京大学大学院工学系研究科電気系工学専攻

37-226541

杜 亜静

Abstract

Spatial light modulators (SLMs) have garnered increasing attention due to their high-resolution control, large-area coverage, flexibility, and compact design, showing extensive applications such as optical communication and imaging technologies. SLMs are essentially two-dimensional free-space electro-optic modulator arrays. Current practical SLMs, primarily based on liquid crystal and MEMS (Micro-Electro-Mechanical Systems) technology, are limited to kHz speeds. Therefore, high-speed, efficient modulation is highly anticipated. Electro-optic (EO) polymers, due to their large electro-optic coefficients and flexibility, are widely used in optical modulators. A high-speed SLM can be achieved by combining electro-optic polymer materials with nanostructures.

In surface-normal modulators, metal gratings have attracted significant interest in EO polymer modulator research. Metal gratings induce plasmonic resonance, achieving high-speed and efficient intensity modulation. Metal gratings also can serve as electrodes for poling and driving voltages. Compared to demonstrated MIM structures, single layer plasmonic grating structures avoid degradation of EO polymer properties during top layer fabrication. However, these modulators still face challenges in high-speed, high-efficiency, and manufacturing robustness.

In this dissertation, we introduce a surface-normal EO polymer modulator using single layer plasmonic grating. The modulator is operating around a 1.55 μm wavelength. The dimerized grating structure selectively excites resonance modes by breaking structural symmetry. Converting to quasi-BIC, a narrow linewidth resonance can be achieved, beneficial for low-voltage resonance shifts. In this system, guided mode resonance is formed through the interaction between the slab waveguide and the metal grating, enhancing light intensity within the EO polymer layer and improving modulation of the incident beam.

The simulation results show that the dimerized grating structure improves the Q factor and robustness compared to unperturbed grating. Additionally, low-voltage

modulation is achieved in plasmonic modulators using dimerized grating structures and enhance modulation efficiency and speed.

Contents

Chapter 1. Introduction

1.1 Introduction of metasurface devices

Metamaterials are composed of periodic subwavelength metal or dielectric structures (i.e., meta-atoms) that exhibit unique electromagnetic responses. The two-dimensional counterpart of metamaterial is metasurface, which demonstrate remarkable electromagnetic wavefront manipulation capabilities due to the interaction between electromagnetic waves and these meta-atom structures as well as their functional arrangements.

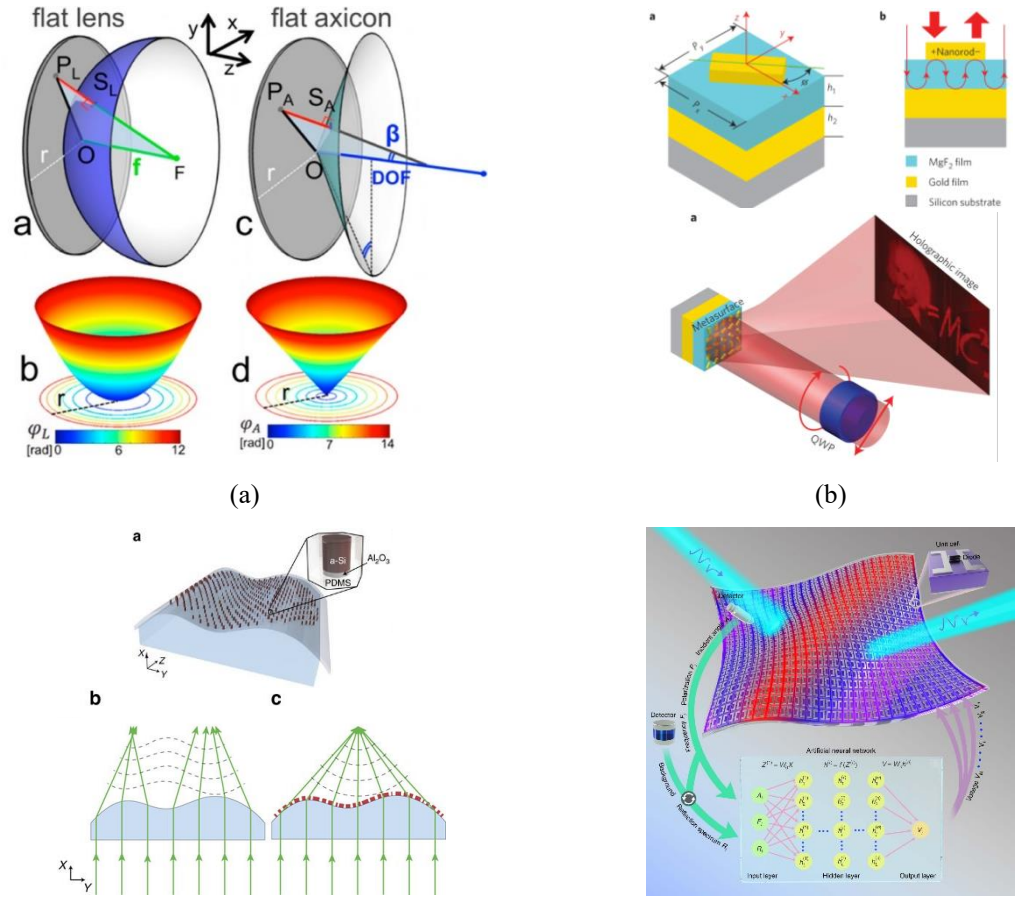

(a) (b)

(c) (d)

Figure 1.1 (a) Schematic showing the design of flat lenses and axicons [3]. (b) Metasurface hologram with MIM structure [4]. (c) Soft metasurface conformed to the surface to re-shape the wavefront and realize the focusing of transmissive electromagnetic wave [6]. (d) Deep-learning-enabled self-adaptive metasurface cloak [7]

Compared to traditional optical elements, metasurface can achieve more efficient

wavefront modulation by altering the amplitude and imparting phase shifts to the incident waves within the subwavelength scale through light-matter interactions. Using metasurfaces, highly practical optical components can be realized in the visible to infrared wavelength range, such as meta-lenses, beam polarizers, holograms, and polarization interfaces.

1.2 Previous work of metasurface modulator

Modulator is a device used to modulate a light beam. Depending on the attribute of the light beam being manipulated, modulators can be classified into intensity modulators and phase modulators. Based on the applications, modulators can also be categorized by the electro-optic (EO) effect, thermo-optic effect, acousto-optic effect, etc. Modulators have widely applications such as wavefront shaping, beam control, and imaging.

By using metasurface, the difficulty of two-dimensional integration with traditional waveguide modulators can be resolved. When light from free space is incident on the metasurface, the interaction between the light and the nano-resonators causes changes in the amplitude, phase, or polarization of the reflected or transmitted light.

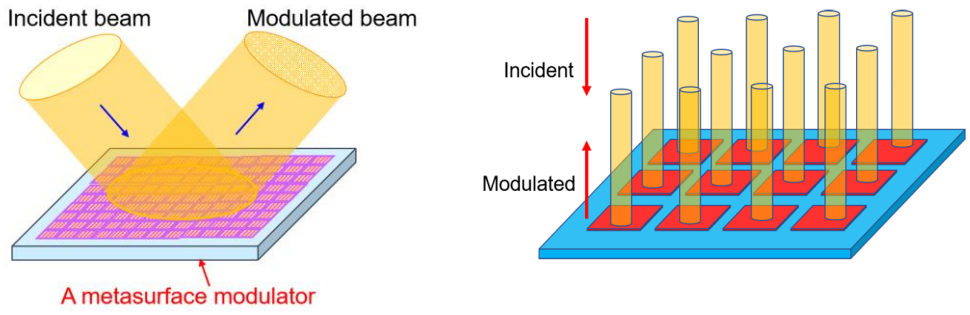

(a) (b)

Figure 1.2 (a) Illustration of metasurface modulators. (b) Illustration of 2D integration of metasurface modulators [1].

There are various materials used for fabricating metasurface modulator, such as lithium niobate, organic polymer, III-V compounds. Next, we will introduce some examples and their modulation performance.

1.2.1 Lithium niobate for electro-optic modulation

Lithium niobate (LN) is a typical electro-optic material with high electro-optic effect and wide optical transparency. An optical modulator based on a lithium niobate ($LiNbO_3$) metasurface combined with a metal grating is introduced [8]. This modulator leverages plasmonic quasi-bound states in the continuum (q-BIC) and guided mode resonance to achieve high-performance optical modulation, offering high-speed modulation.

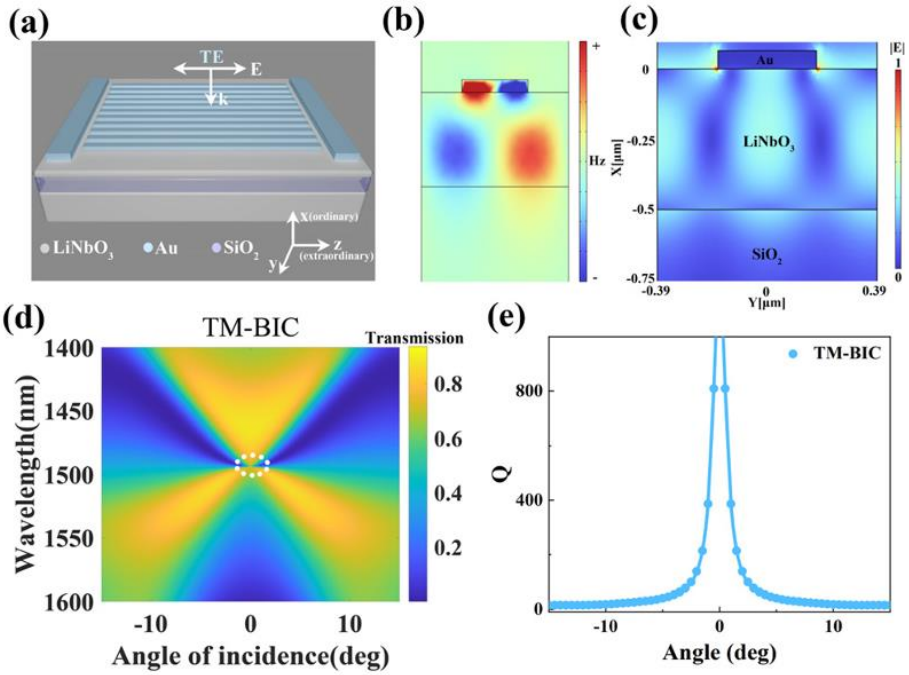

Figure 1.3 The schematic and resonance mechanism in LiNbO3 metasurface modulator [8].

The operating wavelength range of the device is from 1480 nm to 1620 nm, with a maximum resonance depth of approximately 51% at the resonant wavelength. The insertion loss is -2.8 dB at a wavelength of 1510 nm. The dynamic modulation speed reaches up to 190 MHz, and the highest signal-to-noise ratio (SNR) at a frequency of 65 MHz is about 49 dB.

1.2.2 EO polymer for electro-optic modulation

Electro-optic polymers are a class of polymer materials with electro-optic effects, where the refractive index changes when an electric field is applied. The advantages of

organic electro-optic materials include nonlinear coefficients that are higher than traditional materials, high-speed response and can be integrated to any substrate. Considering the layer of metal gratings, they can be basically divided into MIM (metal-insulator-metal) structures and single-layer plasmonic grating structures.

In the single layer plasmonic grating structure, the metal grating is patterned on the substrate, and the EO polymer is coated on top. An electro-optic spatial light modulator (SLM) based on an organic polymer layer, as shown in figure 1.4, utilizing nonlinear organic electro-optic polymer is introduced [9].

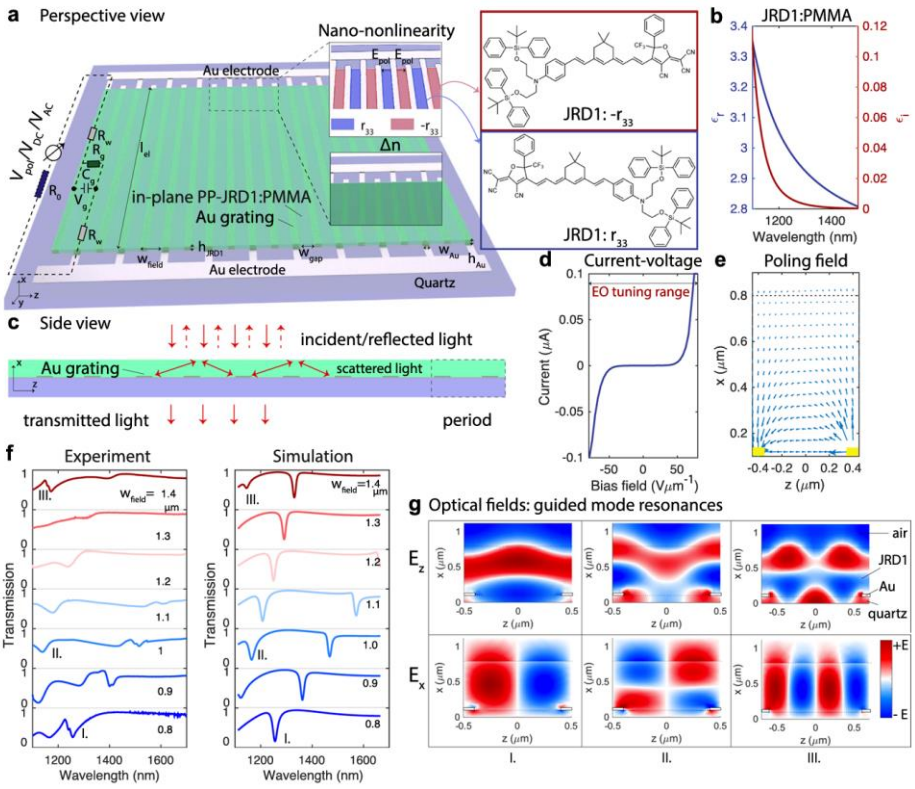

Figure1.4. Schematic view of one-layer plasmonic EO polymer modulator [9]

The modulator combines high-performance electro-optic materials with nanostructure design, exhibiting high modulation efficiency, low power consumption, and high speed. It can achieve a modulation speed of up to 50 MHz, with a maximum modulation depth of 40% in transmission intensity. Using an RF source to drive the modulator and demodulate the transmission intensity through modulation frequency, the application of the broadband Pockels effect, which is 10-100 times higher than

traditional materials, is demonstrated.

In the MIM structure, the metal grating and metal layer act as the counter electrode. As shown in figure 1.5, an electro-optic polymer and silicon nitride hybrid spatial light modulator is proposed, achieving significant EO modulation with high speed and low power consumption [10]. The structure consists of metasurfaces made of periodic SiN arrays, a thin gold layer, and an EO polymer layer. The Au layer and indium tin oxide (ITO) layer serve as electrodes.

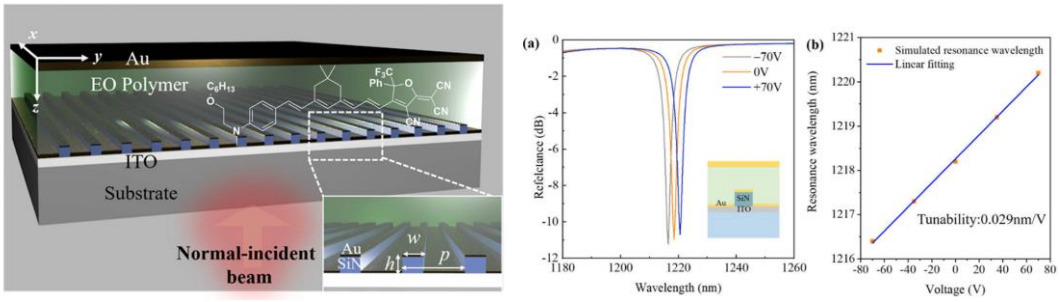

Figure 1.5. Schematic view of MIM EO polymer modulator [10]

The device achieves clear modulation at 10 MHz with a low driving voltage of $V_{p\text{-}p}$=±10 V. By applying different voltages, the resonance wavelength can be tuned, with a tunability of 0.029 nm/V. Most of the optical mode is confined within the EO polymer layer, leading to effective modulation.

1.2.3 III-V compounds for electro-optic modulation

III-V compound materials have multiple advantages when used as electro-optic materials, such as high electron mobility and wide bandgap. A semiconductor-based optoelectronic switch based on active modulation of surface plasmon polaritons (SPPs) is introduced [11]. The SPPD (surface plasmon polariton detector) is composed of a highly p-doped layer and a degenerate n^{++} doped layer, grown on InP substrate. A grating with a period of 2.4 μm couples mid-infrared light into the SPP mode propagating at the junction interface. The modulation capability of the SPP in the mid-infrared wavelength range is demonstrated.

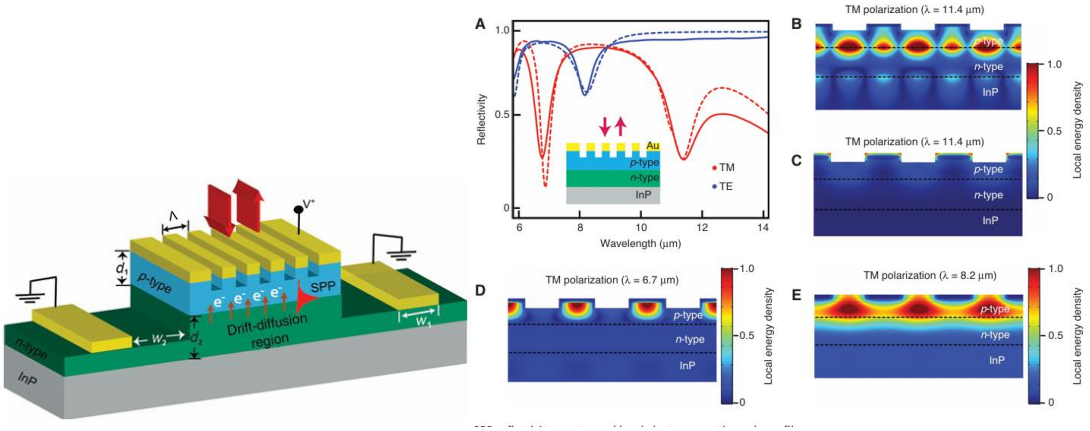

Figure 1.6. Schematic view of surface plasmon polariton diode (SPPD) modulator [11]

Far-field reflectivity modulation was observed under various forward biases, confirming the modulation of SPPs at the junction. The current device architecture supports data rates of up to 1 Gbit/s.

1.3 Introduction of bound state in the continuum (BIC)

In 1929, von Neumann and Wigner predicted the existence of a localized eigenstates of the single-particle Schrödinger equation embedded in the continuum of eigenvalue state solutions. This state is now known as an embedded eigenstate or a Bound State in the Continuum (BIC). These states coexist with the surrounding continuum states but remain localized without radiative loss due to symmetry or interference effects, giving BICs theoretically infinite quality factors and superior optical properties in practical applications. In ideal systems, any perturbation would cause a BIC to collapse into a Fano resonance with a finite lifetime, known as a quasi-BIC state, which is usually the state realized in practical implementations.

As shown in figure1.7, in an open system, the spectrum consists of a continuum of extended states (blue line) and discrete bound states (green line) that have no outgoing radiation. The spatial localization of the bound states is caused by the confining structure or potential (black dashed line). States within the continuum typically couple to the extended waves and radiate, becoming leaky resonant states (orange). However, bound states in the continuum (BICs; red line) are special states that exist within the

continuum but remain localized and do not radiate [12].

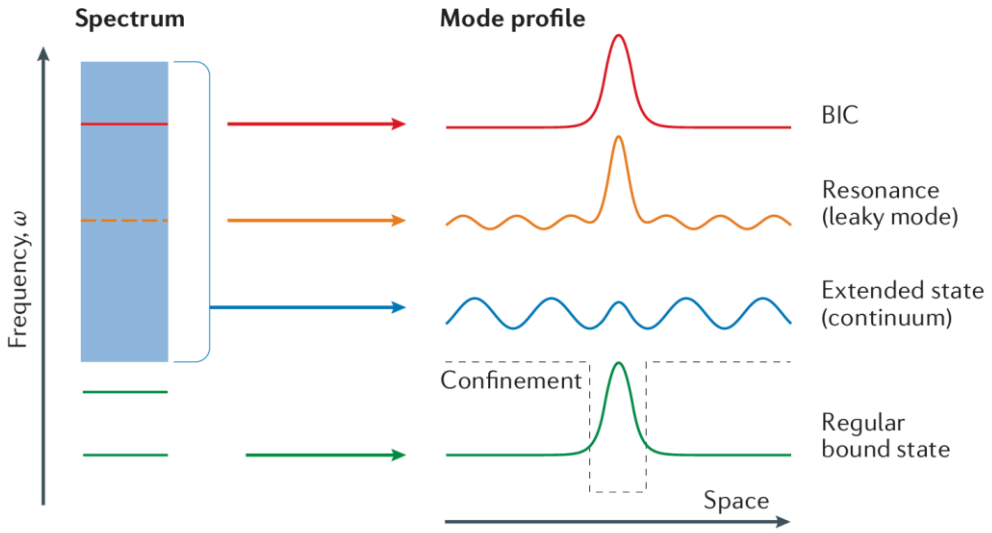

Figure 1.7 Illustration of a BIC [12]

BIC structures are naturally high-quality factor resonators due to Q is infinite in the ideal case. Thus, BIC structure has promising application in many optical and photonics applications. We focus on the two most prevalent cases: symmetry-protected BICs and interference-based BICs.

1.3.1 Symmetry-protected BIC

When a state cannot be coupled to leakage modes due to a symmetry mismatch, this state meets the BIC criterion for symmetry protection. As a result, the state behaves as a bound state and does not radiate even in the continuous spectral band. By breaking the symmetry of the structure, the symmetry-protected BIC (SP-BIC) can be perturbed and transformed into a quasi-BIC. This interference between a discrete localized quasi-BIC and a continuum band of states results in a characteristic Fano resonance line-shape in the transmission spectrum with a considerable high-quality factor. Symmetry-protected BICs are widely used in ultrafast optical operation, imaging, and low-threshold lasers. Figure 1.8 shows an example of SP quasi-BIC. In this example, controlling symmetry breaking by tilting the particle long axis realizes SP-qBIC.

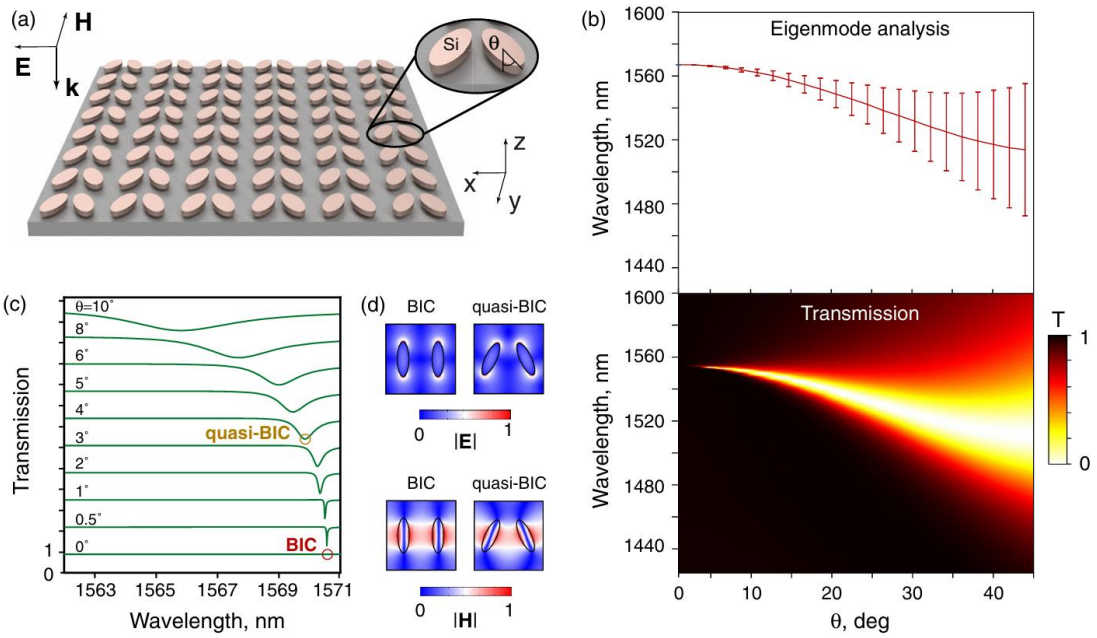

Figure 1.8 A typical SP-qBIC dielectric metasurface composed of ellipsoid nanoparticles [17]

1.3.2 Interference-based BIC

By tuning the parameters within resonant structures, destructive interference in individual radiation channels can be induced, leading to the formation of interference-based BICs. Achieving interference cancellation requires that the number of tuning parameters exceed the number of radiation channels. However, as the number of parameters increases, the tuning process becomes increasingly complex, making this method more effective when fewer radiation channels are present. Based on the spatial relationship between resonant cavities, interference-based BICs can be subdivided into Fabry-Pérot (F-P) BIC and Friedrich-Wintgen (FW) BICs.

Fabry-Pérot (F-P) BIC arises from destructive interference between two resonant cavities separated by a specific distance.When connected to a single radiation channel, an F-P BIC can be established by adjusting the distance between two resonant structures to accumulate a phase shift equal to an integer multiple of 2π [13].

Friedrich-Wintgen (FW) BICs are generated by the destructive interference of two or more resonant modes within the same cavity. With a specific continuous parameter varies, the mode interference induces an avoided crossing of the two resonances. At a

particular parameter value, the width of one resonance vanishes, resulting in an FW BIC. Meanwhile, the other resonance becomes more lossy and has a maximal width. Figure 1.9 shows an example of FW-BIC. In this example, an FW BIC is generated through the interference between FPR and GMR modes under coherent phase matching conditions [16].

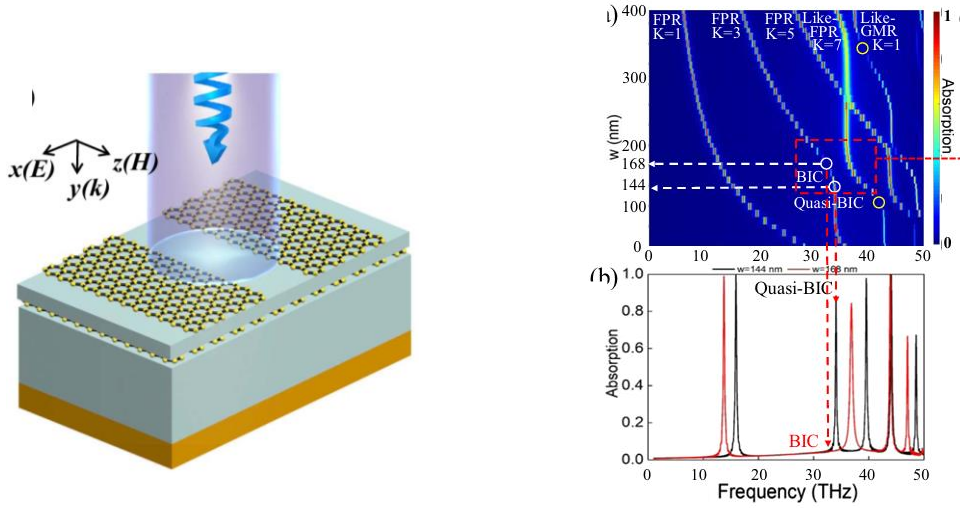

(a) (b)

Figure 1.9 (a) 3D schematic diagram composed of graphene gratings (b) BIC formation in the hybrid FPR–GMR system [16]

1.4 Purpose of this research

When utilizing the electro-optic effect for free-space modulation, a narrow-linewidth resonance is advantageous for fully shifting the resonance point with minimal applied voltage. Intensity modulation is achieved in the plasmonic modulator, aiming for high speed, high efficiency and low drive-voltage. In this research, a perturbation is introduced to induce Fano resonance and achieve narrow-linewidth resonance for electro-optic modulation. Through simulations, the Q factor in the single layer plasmonic grating modulator is enhanced and the robustness improvement of manufacturing is demonstrated.

Chapter 2. Theory

2.1 Pockels effect

When electric field is added to material, the change in the refractive index is related to the magnitude of the electric field strength. This phenomenon is known as the electro-optic effect and the material is called an electro-optic material. The electro-optic effect can be simply expressed as

$$\Delta n = rE + \kappa E^2 \tag{2.1}$$

The first term on the right side of (2.1) is called the linear electro-optic effect or Pockels effect. The second term is proportional to the square of the electric field strength and is known as the nonlinear electro-optic effect or Kerr effect. For most materials, the Kerr effect is much smaller than the Pockels effect, so here we will only discuss the Pockels effect.

From the classical atomic Lorentz model, it is known that a nonzero second-order nonlinear polarizability tensor can exist only in materials without an inversion center of symmetry quantities. Therefore, the electro-optical effect also arises only in materials without inversion symmetry centers.

If the amplitude of the DC electric field is set as $\boldsymbol{E}^0$ and the complex amplitude of the optical field with frequency ω be $\boldsymbol{E}$. The relationship between $\boldsymbol{E}^0$ and $\boldsymbol{E}$ can be expressed as

$$\boldsymbol{E}(0, \boldsymbol{r}, t) = \boldsymbol{E}^0 \tag{2.2}$$

$$\boldsymbol{E}(\omega, \boldsymbol{r}, t) = \frac{1}{2}(\boldsymbol{E}e^{-i\omega t} + c.c.) \tag{2.3}$$

To analyze the variation of the refractive index of light with frequency ω, only the polarization intensity components which has the same frequency as the optic field are considered. The first order and second order of the polarization intensity can be expressed as

$$P_i^{(1)}(\omega) = \varepsilon_0 \chi_{ij}(\omega) E_j \tag{2.4}$$

$$P_i^{(2)}(\omega) = \varepsilon_0 \chi_{ijk}(\omega, 0) E_j E_k^0 \tag{2.5}$$

So, the electric displacement can be expressed as

$$\boldsymbol{D} = \varepsilon_0 \boldsymbol{E} + \boldsymbol{P}_L + \boldsymbol{P}_{NL} = \varepsilon_0 \varepsilon \cdot \boldsymbol{E} + \boldsymbol{P}_{NL} = \varepsilon_0 \varepsilon' \cdot \boldsymbol{E} \tag{2.6}$$

ε is relative permittivity and ε' is equivalent relative permittivity after applying voltage. The components of the electric displacement can be expressed as

$$D_i = \varepsilon_0 \varepsilon_{ij} E_j + \varepsilon_0 \chi_{ijk}(\omega, 0) E_j E_k^0 = \varepsilon_0 \varepsilon_{ij}' \cdot E_j \tag{2.7}$$

The relative dielectric constant is changed after the addition of voltage. The amount of change can be expressed as

$$\Delta \varepsilon_{ij} = \chi_{ijk}(\omega, 0) E_k^0 \tag{2.8}$$

It is obvious that the amount of change $\Delta \varepsilon_{ij}$ is proportional to the electric field strength and is related to the second order polarizability.

When the electric field $\boldsymbol{E}^0$ is added, the dielectric constant and refractive index of the medium will change, so the refractive index ellipsoid can be expressed in a more general form:

$$\frac{1}{n_1^2} x^2 + \frac{1}{n_2^2} y^2 + \frac{1}{n_3^2} z^2 + 2 \frac{1}{n_4^2} yz + 2 \frac{1}{n_5^2} xz + 2 \frac{1}{n_6^2} xy = 1 \tag{2.9}$$

When the electric field is zero, the dielectric spindle is parallel to the laboratory axes x, y and z, respectively.

Since generally $n^2 = \varepsilon$, the change in refractive index can be solved for by solving for the change in the dielectric constant. By solving the change in the dielectric constant and its inverse induced by DC field, $\Delta \varepsilon$ and $\Delta \varepsilon^{-1}$, we can derive that

$$\Delta \varepsilon_{ij}^{-1} = \frac{-\chi_{ijk}(\omega; \omega, 0) E_k^0}{\varepsilon_{ii} \varepsilon_{jj}} \tag{2.10}$$

Assume

$$\gamma_{ijk} = \frac{-\chi_{ijk}(\omega; \omega, 0)}{\varepsilon_{ii} \varepsilon_{jj}} \tag{2.11}$$

Then equation (2.10) can be derived as

$$\Delta \varepsilon_{ij}^{-1} = r_{ijk} E_k^0 \tag{2.12}$$

Here, r_{ijk} is defined as the electro-optic coefficient. Considering the complete reciprocal symmetry and the time-reversal symmetry, the electro-optic coefficient is reciprocal for the footmarks *i* and *j*, $r_{ijk} = r_{jik}$.

Based on this symmetry, the footmarks *i* and *j* in the electro-optic coefficients r_{ijk} are mergeable, and the merging rules are tabulated below.

l	1	2	3	4	5	6
jk	*xx*	*yy*	*zz*	*yz(zy)*	*zx(xz)*	*xy(yx)*

Table 2.1 Electro-optical coefficients footmark labels merging rule

Therefore, the number of independent components of the electro-optic coefficient is 18, and it will decrease after considering the spatial symmetry of matter. After combining the footnotes, equation (2.12) can be written as

$$\Delta\varepsilon_{ij}^{-1} = r_{lk}E_k^0 \tag{2.13}$$

Considering the relationship between dielectric constant and refractive index,

$$\Delta\left(\frac{1}{n_i^2}\right) = \Delta\varepsilon_{ij}^{-1} = r_{lk}E_k^0 \tag{2.14}$$

Thus, the change in the refractive index ellipsoid constant due to the electric field can be expressed in the following matrix form,

$$\begin{bmatrix} \Delta(\frac{1}{n_1^2}) \\ \Delta(\frac{1}{n_2^2}) \\ \Delta(\frac{1}{n_3^2}) \\ \Delta(\frac{1}{n_4^2}) \\ \Delta(\frac{1}{n_5^2}) \\ \Delta(\frac{1}{n_6^2}) \end{bmatrix} = \begin{bmatrix} r_{11} & r_{12} & r_{13} \\ r_{21} & r_{22} & r_{23} \\ r_{31} & r_{32} & r_{33} \\ r_{41} & r_{42} & r_{43} \\ r_{51} & r_{52} & r_{53} \\ r_{61} & r_{62} & r_{63} \end{bmatrix} \begin{bmatrix} E_x \\ E_y \\ E_z \end{bmatrix} \tag{2.15}$$

2.2 EO polymer

2.2.1 Introduction of EO polymer

Typical electro-optic polymers generally consist of an active component (chromophore) and an inert component (polymer matrix). For EO polymers, the most important component is the dipole chromophore, which has a strong second-order nonlinear optical effect. Chromophore is composed of three parts, the electron donor (e-Donor), π-conjugated electron bridge (π-Conjugated), and electron acceptor (e-Acceptor).

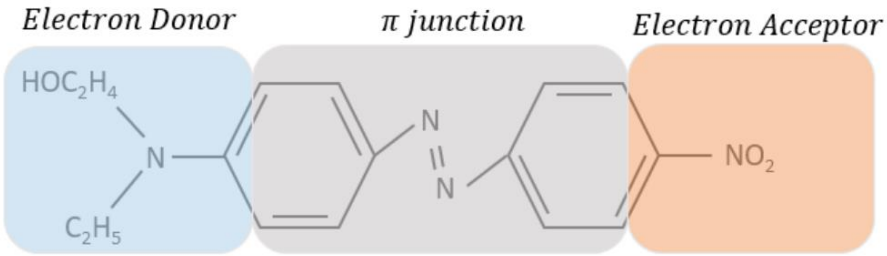

Figure 2.1. Illustration of a typical D-π-A chromophore

Chromophore molecules usually tend to be arranged symmetrically, so that the material does not exhibit macroscopic nonlinear properties. To exhibit electro-optical effects, the polymer is usually polarized electrically or optically at a high temperature to obtain uniformly orientation of the chromophores under the effect of polarization. After polarization is completed, the chromophore orientation is back to an unmovable state by cooling down. So, the polymer becomes an anisotropic electro-optic polymer. The poling process is shown in Figure 2.2.

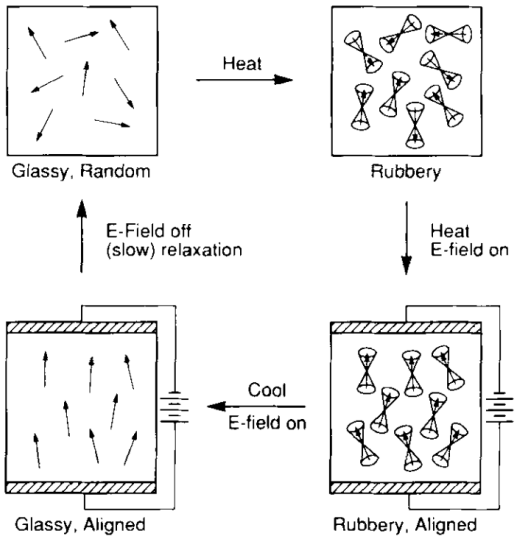

Figure 2.2. Schematic representation of the poling process [23]

2.2.2 Linear electro-optic effects in polarized electro-optic polymers

The second-order susceptibility of centrosymmetric materials is zero. Therefore, polymers usually need to be treated in a certain way to break their central symmetry, such as applying a strong external electric field for poling. Typically, in experiments, the poling electric field is applied perpendicular to the surface of the polymer. So, the principal axis of the poled film is chosen as the z-axis.

After poling, the polymer exhibits a uniaxial crystal structure, $n_1 = n_2 = n_0$, $n_3 = n_e$. n_0 and n_e are correspond to the ordinary and extraordinary light incidence conditions, respectively. Based on symmetry considerations, the non-zero element of the second-order susceptibility is $\chi^{(2)}_{333}$, $\chi^{(2)}_{113} = \chi^{(2)}_{223}$, $\chi^{(2)}_{131} = \chi^{(2)}_{232}$, $\chi^{(2)}_{311} = \chi^{(2)}_{322}$. According to the relationship between electro-optic coefficients and the second-order nonlinear susceptibility, the non-zero element of the electro-optic coefficient is r_{33}, $r_{51} = r_{42}$, $r_{13} = r_{23}$. According to Kleiman symmetry, $r_{42} = r_{13}$. Therefore, its electro-optic coefficient matrix is:

$$\begin{bmatrix} 0 & 0 & r_{13} \\ 0 & 0 & r_{13} \\ 0 & 0 & r_{33} \\ 0 & r_{13} & 0 \\ r_{13} & 0 & 0 \\ 0 & 0 & 0 \end{bmatrix} \tag{2.16}$$

The DC electric field is usually applied along the z-axis, $E_x = E_y = 0,\ E_z = E^0$. According to equation (2.14),

$$\Delta\left(\frac{1}{n_1^2}\right) = r_{13}E_z \tag{2.17}$$

$$\Delta\left(\frac{1}{n_2^2}\right) = r_{13}E_z \tag{2.18}$$

$$\Delta\left(\frac{1}{n_3^2}\right) = r_{33}E_z \tag{2.19}$$

Due to $\Delta\left(\frac{1}{n^2}\right) = -\frac{2}{n^3}\Delta n$, so

$$\Delta n_o = -\frac{{n_o}^3}{2} r_{13}E_z \tag{2.20}$$

$$\Delta n_e = -\frac{{n_e}^3}{2} r_{33}E_z \tag{2.21}$$

When light propagates in the EO polymer, the refractive index ellipsoid can be expressed as

$$\left(\frac{1}{n_o^2} + r_{13}E_z\right)(x^2 + y^2) + \left(\frac{1}{n_e^2} + r_{33}E_z\right)z^2 = 1 \tag{2.22}$$

Under moderate poling conditions, the medium is approximately isotropic. Thus, the electro-optic coefficients have the approximate relationship.

$$r_{33} = 3r_{13} \tag{2.23}$$

2.2.3 Advantages of EO polymer

The electro-optical effect, as mentioned before, is the phenomenon of a change in refractive index in non-linear optical crystals or non-linear organic polymers due to the applied electric field.

The main electro-optical materials commonly used are:

(1) $LiNbO_3$

Lithium niobate is a commonly used ferroelectric crystal material which is widely used in the production of optoelectronic devices. Lithium niobate optical waveguides have the advantages such as strong Pockels effect, high-speed response, low thermo-optic coefficient and excellent chemical and mechanical stability. However, conventional $LiNbO_3$ modulators are bulky and not easily integrated with other photonic components. In addition, the high driving voltage leads to high energy consumption.

(2) III-V semiconductors

The family of III-V semiconductors include compounds between group-III (Al, Ga, In) and group-V (N, P, As, Sb) elements of the periodic table. The most important representatives are the binary compounds GaAs, InP, GaP, and GaN as well as the ternary InGaAs, InGaP and the quaternary InGaAsP, InGaAlP semiconductors. III-V semiconductors exhibit multiple EO effects, such as linear EO effect, Franz–Keldysh effect, and free-carrier effects. Although the EO coefficient is not so high, the higher refractive index can partially compensate for the weaker EO coefficient, while their lower dielectric constant also allows for easier phase-matching in traveling wave designs. However, the cost is generally more expensive than silicon and it requires complex fabrication processes, especially for quantum well structures.

(3) Organic electro-optical polymers

Electro-optic polymer modulators have advantages such as high EO coefficients, fast response and can be integrated to any substrate. In general, the refractive index of organic polymers ranges from 1.5 to 1.7 [27]. The transmission loss of organic polymer light waveguides now can be achieved at <3 dB/cm. According to recent reports, the electro-optical coefficients of electro-optical polymers have reached r_{33} =735pm/V, and their transmission losses are comparable to lithium niobate [28]. However, EO polymers can degrade over time and are sensitive to environmental conditions.

The comparison of GaAs, $LiNbO_3$ and EO polymer properties is shown in table 2.2.

Materials	$LiNbO_3$	GaAs	EO Polymer
EO coefficient (pm/V)	31	1.5	735
Refractive index n	2.2	3.5	1.6-1.7
Performance index n^3r (pm/V)	340	64	584
Dielectric constant ε	28	12	3.5
Loss (dB/cm)	0.2	2	0.2-1.1
V_π (V)	5-7	5-7	1.2-1.8
Bandwidth (GHz)	40	50	>100

Table 2.2. Comparison of GaAs, $LiNbO_3$ and EO polymer properties

2.3 Guided mode resonances for dimerized grating

Guided mode resonance (GMR) is an optical phenomenon that occurs in waveguides with periodic structures. When the frequency and angle of the incident light match the guided modes of the waveguide, the incident light is coupled into the guided modes of the waveguide, resulting in strong optical resonance. This resonance produces sharp reflection or transmission peaks, known as guided mode resonance.

The refractive index of the EO polymer is higher than that of the air above and the substrate below, thus forming a slab waveguide. Guided mode resonances can be formed through the interaction between the slab waveguide and the metal grating.

For unperturbed grating, when the electric field is polarized in the xz plane (TM polarization), the system supports two eigenmodes around the wavelength of approximately 1500 nm, which cannot be excited by external plane waves. In this mode, the optical field alternates direction at metal strip, and it can be considered as band-edge modes at the X point of the irreducible Brillouin zone of a one-dimensional system as shown in figure. 2.3. Blue solid lines are the lowest-order mode of the slab without the metal grating, and open circles are the modes with the presence of the grating. The mode profiles of the E_z component at the band edges are shown on the right of figure 2.3(a). With the introduction of the metal grating (open circles), a band gap is opened. Despite the dissipative losses in the metal and EO polymer, the modes below the light

line remain guided modes. For $k_x = \pi/a$, these modes have a wavelength of 2a and form standing waves. The electric field associated with the lower band-edge mode is strongly concentrated in the metal regions, while the upper band-edge mode's electric field is located between the metal strips, orthogonal to the lower band-edge mode.

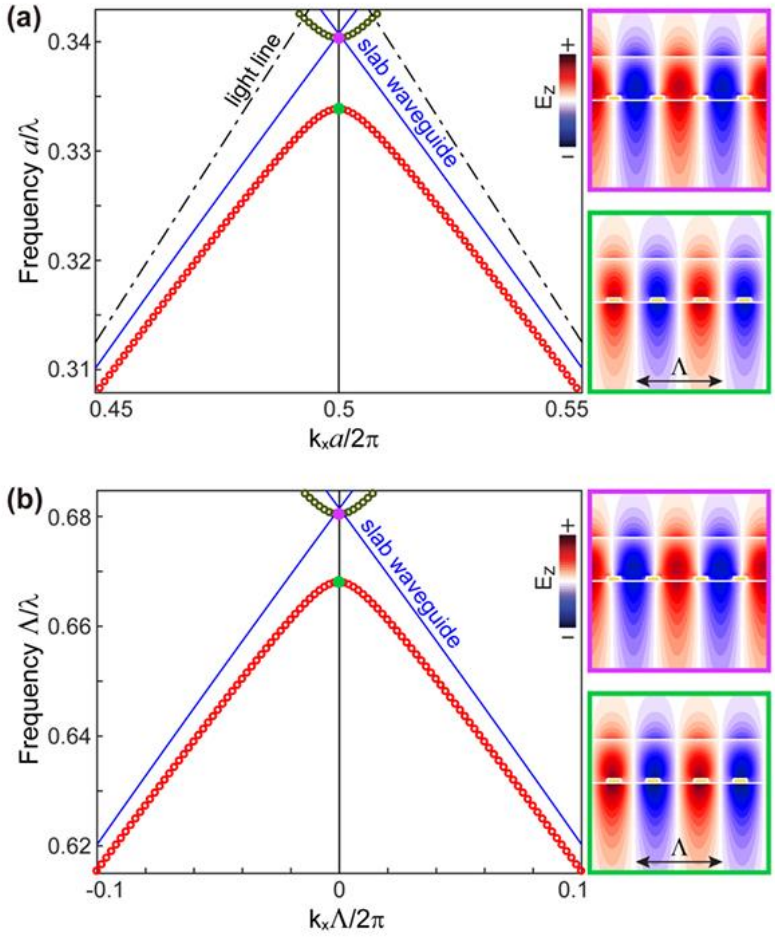

Figure 2.3 Band diagram of a slab with (a) unperturbed grating and (b) gap dimerized grating [35]

To enable these modes to be excited by external plane waves, perturbations can be introduced by making the distance between the grating or the widths of the grating unequal, thus reducing the symmetry of the system. This shifts the target modes to the center of the irreducible Brillouin zone.

The transmission spectra are shown in figure 2.4. By examining the field distributions at the transmission dips, resonance modes are identified as M1(d_1=d_2) and M2(w_1=w_2). Among these two resonances, only one can be excited under normal

incidence, while the other remains in a dark state if only one parameter is dimerized.

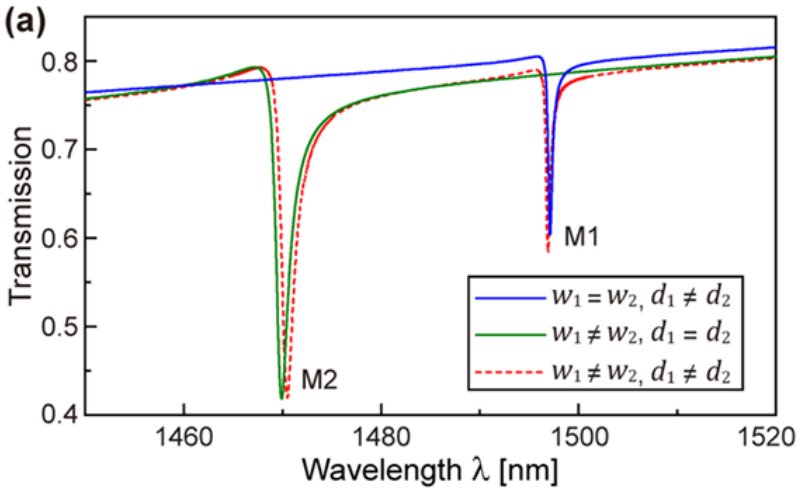

Figure 2.4 Transmission spectra at normal incidence for either nonequal distance or nonequal width [35].

2.4 Q factor of dimerized grating

As mentioned in previous section, by breaking the symmetry of structures, SP-BIC can be perturbed and then transformed into quasi-BIC. Figure 2.5 illustrates a schematic of the unperturbed grating and the dimerized grating.

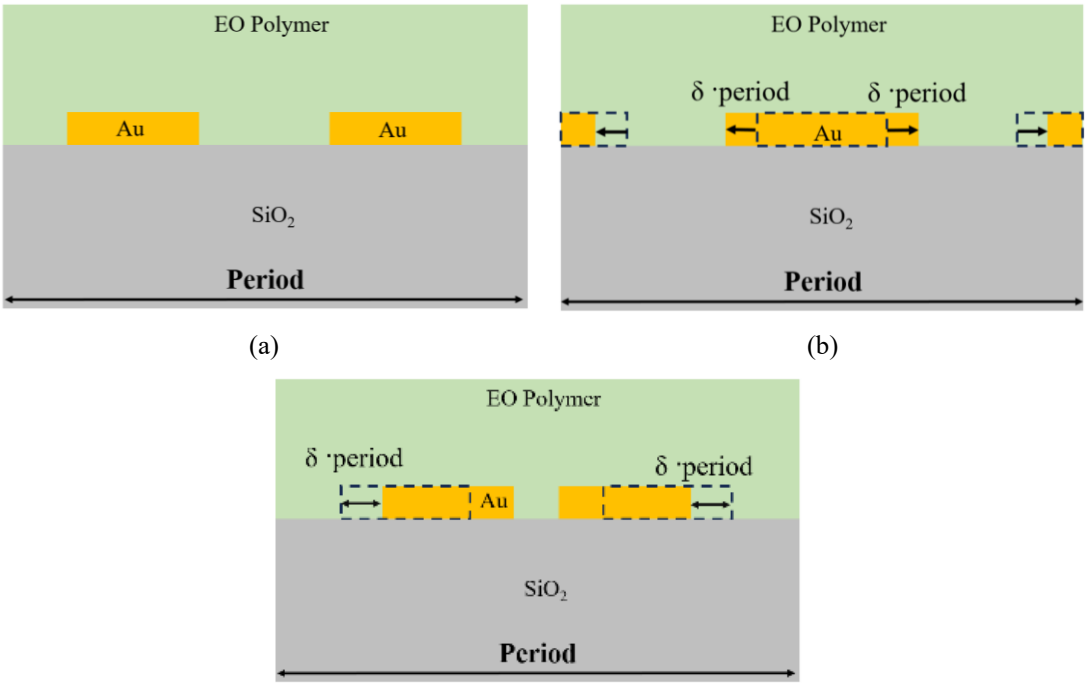

Figure 2.5. Cross-section of (a) Unperturbed grating (b)Width dimerized grating (c) Gap dimerized grating

From the temporal coupled-mode theory (TCMT), the relationship between the Q-factor and the coupling strength is

$$Q_{ext} \propto \frac{1}{|c_y(k)|^2} \tag{2.24}$$

Therefore, if we know the relationship between the perturbation δ and the coupling coefficient, the relationship between the Q-factor and the perturbation can be derived.

For TE polarized light, the electric field can be expressed as:

$$E_{z,n}(k_x, x, y) = u^{(0)}_{k_x,n}(x, y)\exp(ik_x x) \tag{2.25}$$

in which $E_{z,n}$ is the z-direction component of the electric field, and $u^{\square}_{k_x,n}$ is the Bloch wave component without the perturbation. In the perturbation theory, when perturbation is applied, the eigenvalue equation with Bloch functions as eigenvectors can be expressed as

$$(\Omega + V)u^{\square}_{k_x,n} = \beta^2_{k_x,n}u^{\square}_{k_x,n} \tag{2.26}$$

in which $\beta_{k_x,n}$ is the wavenumber, V is the perturbation operator. When the x is very

small, the perturbation operator V can be approximated as $V \cong -\frac{\delta\varepsilon_r}{\varepsilon_r}\Omega$.

The eigenvector can be expressed as the sum of the unperturbed eigenvector and the perturbed eigenvector

$$u_{k_x,n} = u_{k_x,n}^{(0)} + u_{k_x,n}^{(1)} \tag{2.27}$$

The first-order perturbation component can be expressed using the unperturbed eigenvector as

$$u_{k_x,n}^{(1)} = \sum_{m\neq n} \frac{\int (u_{k_x,m}^{(0)}) * V u_{k_x,n}^{(0)}}{\beta_{k_x,m} - \beta_{k_x,n}} u_{k_x,m}^{(0)} \tag{2.28}$$

$u_{k_x,m}^{(0)}$ is a mode that is capable of coupling to free space and is often referred to the "bright mode". $u_{k_x,n}^{(0)}$ is a mode which is not coupled to free space and is often called the "dark mode".

The coupling degree to free space is quantified by the Fourier coefficients when the mode is expanded in spatial frequency. The coupling degree for wavenumber k can be expressed as 2.29. $\langle\rangle$ represents the spatial average.

$$c_n(k) = \langle u_{k_x,n}^{(0)} \rangle + \langle u_{k_x,n}^{(1)} \rangle \tag{2.29}$$

Since the dark mode in the unperturbed state cannot couple to free space, so

$$\langle u_{k_x,n}^{(0)} \rangle = 0 \tag{2.30}$$

Therefore, the coupling degree is

$$c_n(k_x) = \langle u_{k_x,n}^{(1)} \rangle = \sum_{m\neq n} \frac{\int (u_{k_x,m}^{(0)}) * V u_{k_x,n}^{(0)}}{\beta_{k_x,m} - \beta_{k_x,n}} \langle u_{k_x,m}^{(0)} \rangle \tag{2.31}$$

The coupling coefficient $C_{m,n}$ represents the interaction strength between the dark mode and the bright mode. The coupling coefficient and wavenumber can be written as

$$C_{m,n} = \int (u_{k_x,m}^{(0)}) * V u_{k_x,n}^{(0)} \tag{2.32}$$

$$\Delta\beta_{m,n} = \beta_{k_x,m} - \beta_{k_x,n} \tag{2.33}$$

By applying perturbation through the grating, the interaction between two modes allows the dark mode to couple with free space, causing the coupling coefficient $C_{m,n}$

to become non-zero. Therefore, the mode $u_{k_x,n}^{(1)}$ that is first excited in the dimerized grating can couple with free space.

After considering the spatial distribution of the electric field and the perturbation V, the coupling coefficient $C_{m,n}$ in dimerized grating can be expressed as

$$C_{m,n} = 4V_0F_1\delta_L \tag{2.34}$$

F_1 is the Taylor expansion term of indefinite integral of the resonance produced by the anti-bonding mode. Therefore, the dependence of the Q-factor on the perturbation δ can be expressed as:

$$Q \propto \frac{1}{{\delta_L}^2} \tag{2.35}$$

Thus, the Q-factor resulting from resonance coupling is inversely proportional to the square of the perturbation.

2.5 Proposed modulator structure

Figure 2.6 shows the schematic view of the proposed structure. A gold grating is patterned on the substrate, coating with EO polymer. The EO polymer has a higher refractive index compared to the air above and the substrate below, forming a planar waveguide. The gold grating can induce plasmonic resonances and serve as electrodes for applying driving voltages. Applying electric field to the gold electrodes will induce changes in refractive index due to the Pockels effect.

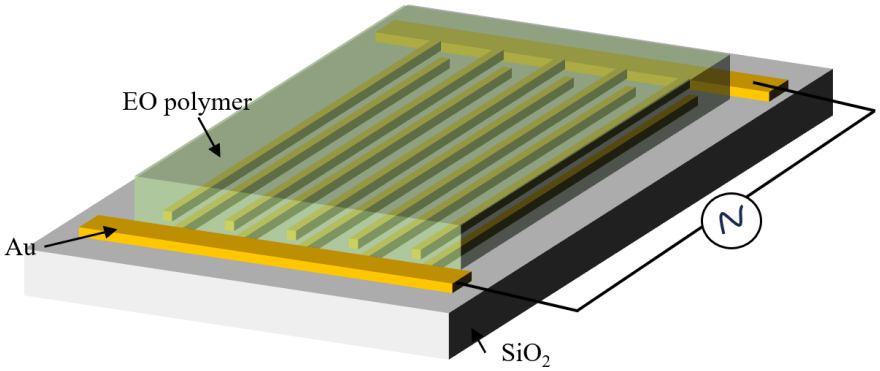

Figure 2.6. Schematic view of the proposed EO polymer modulator with single gold layer

The proposed structure introduces a dimerized grating into the sub-wavelength grating. By introducing the dimerized grating, the Q-factor of the resonance can be controlled through perturbation. The introduction of the dimerized grating brings in quasi-BIC, enabling narrow linewidth resonance for electro-optic modulation and enhancing the Q factor of the resonance. Additionally, due to the very low resistivity of gold, the RC time constant is reduced, leading to faster modulation bandwidth. Since the adjacent gold gratings are also used as electrodes, the driving voltage is very low.

Chapter 3. Numerical simulation

3.1 Introduction of FDTD method

The Finite-Difference Time-Domain (FDTD) method is a numerical analysis technique used to model computational electrodynamics, finding approximate solutions to systems of related differential equations. As a time-domain method, FDTD allows for simultaneous computation over multiple frequency ranges within a single simulation run and can naturally accommodate a wide range of linear material properties. The essence of FDTD is to change the time-dependent Maxwell's rotational equations to a discrete-difference form, dividing the continuous space into finite grid cells (Yee cell) for computation. The higher the number of grid cells, the more accurate the calculation results.

The calculation process primarily involves solving for the electric field vector components in the spatial volume at a given point in time, then calculating the magnetic field vector components in the same spatial volume at the next time step and iterating this cycle. Continuous cyclic calculations are performed in both the spatial and temporal domains, ultimately yielding more accurate transient or steady-state electromagnetic field results. Using FDTD, the polarization and wavelength-dependent interactions of light with various materials and structures can be thoroughly studied. Optical phenomena such as reflection, transmission, diffraction, interference, and absorption can be analyzed in detail.

3.2 Plasmonic grating modulator

In the simulation, the refractive index of the EO polymer is set as n_{EO} = 1.65, the refractive index of gold (Au) is used from the Johnson and Christy in Lumerical refractive index data, and the perturbation is set as δ.

3.2.1 Device design

In this section, the proposed EO polymer modulator with dimerized single layer

plasmonic grating is analyzed. We introduce the dimerized grating to achieve narrow linewidth resonance for electro-optic modulation and want to verify its improvement of the Q factor and robustness.

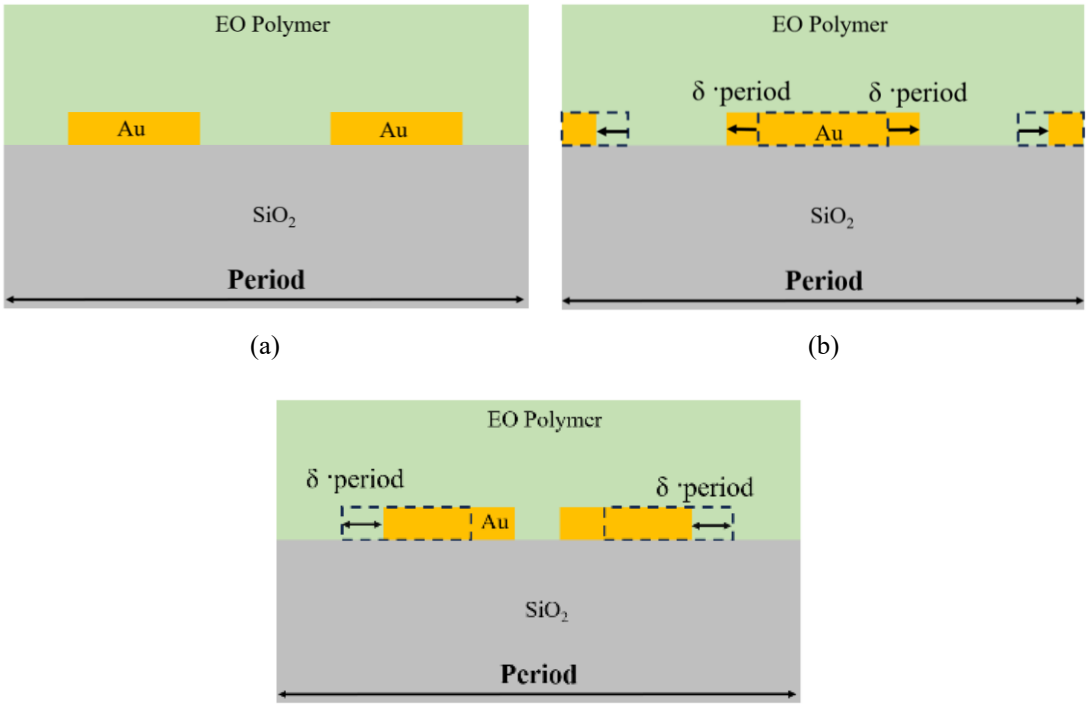

Figure. 3.1 Cross sectional illustrative image of (a)unperturbed plasmonic grating, (b)width dimerized grating (c)gap dimerized grating.

As described in principle, dimerized gratings include two types, width dimerized grating that grating width unequal and gap dimerized grating that gap width unequal as shown in figure. 3.1(b)(c). This section will compare these two types dimerized grating with the unperturbed grating as shown in figure 3.1(a).

3.2.2 Transmittance property

The dispersion relation of the modes can be approximated by calculating the transmittance spectrum of the grating at different periods. At a specific wavelength, the frequency of the incident light matches the natural frequency of the resonator, resulting in resonance. By calculating the transmittance spectrum, the resonance of the coupling can be resolved.

Perturbation is introduced to induce Fano resonance. When the structure changes, the Fano parameter q also changes. If an external perturbation does not couple to the continuum of states, we obtain the Fano parameter $q \to \pm\infty$ and the Fano lineshape becomes a symmetric Lorentzian function. When the external perturbation does not couple to the discrete state, the Fano profile becomes a symmetric quasi-Lorentzian anti-resonance in the continuum spectrum $q = 0$, and it appears as a true zero in the spectrum.

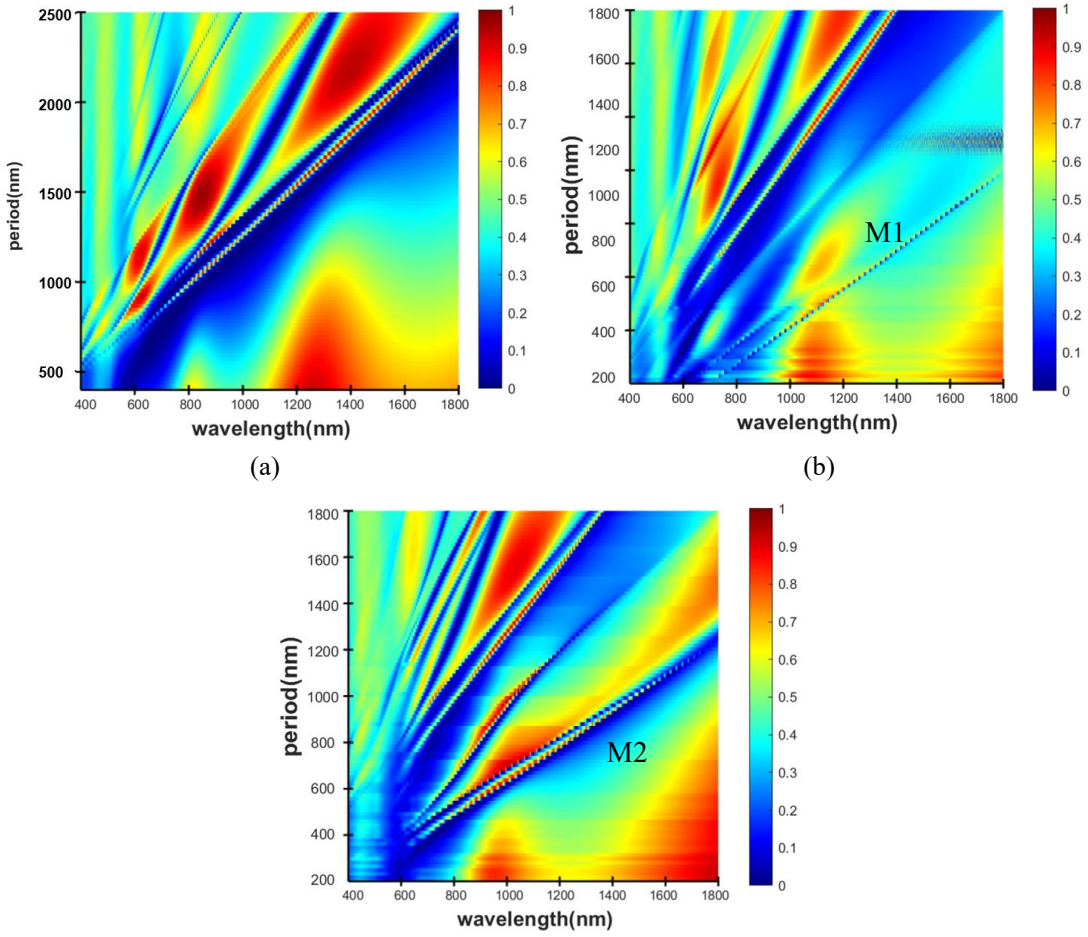

Figure. 3.2 Simulation transmission spectrum of (a)unperturbed grating (b)gap dimerized grating (c)width dimerized grating ((a):FF=s/Λ=0.5 EO polymer thickness=550nm, (b):FF=s/Λ=0.5 EO polymer thickness =550nm δ=0.055, (c):FF=s/Λ=0.5 EO polymer thickness =550nm δ=0.05)

Figure 3.2 shows the transmittance spectrum for gratings with and without perturbations at different periods. Compared to the unperturbed grating in Figure 3.2(a),

the perturbed gratings in Figures 3.2(b) and (c), the width dimerized grating and the gap dimerized grating, exhibit resonances induced by the M1 and M2 modes. The perturbed gratings show sharp resonances with narrow linewidths compared to the unperturbed grating.

By adjusting the period, the resonance can be tuned to the desired wavelength. If we want to get resonance near a wavelength of 1550nm, the period is chosen to be around 2000 nm in the unperturbed grating structure and around 1000 nm in the gap and width dimerized structure.

3.2.3 Mode profile

Figure 3.3 shows the optical resonance modes excited by a normally incident plane wave. In TM light, modes where the antinode of the H_y distribution coincides with the perturbation center will couple, as shown in Figures 3.3(a) and (b). Furthermore, according to Maxwell's equations, the electric field forms vortices around the magnetic field.

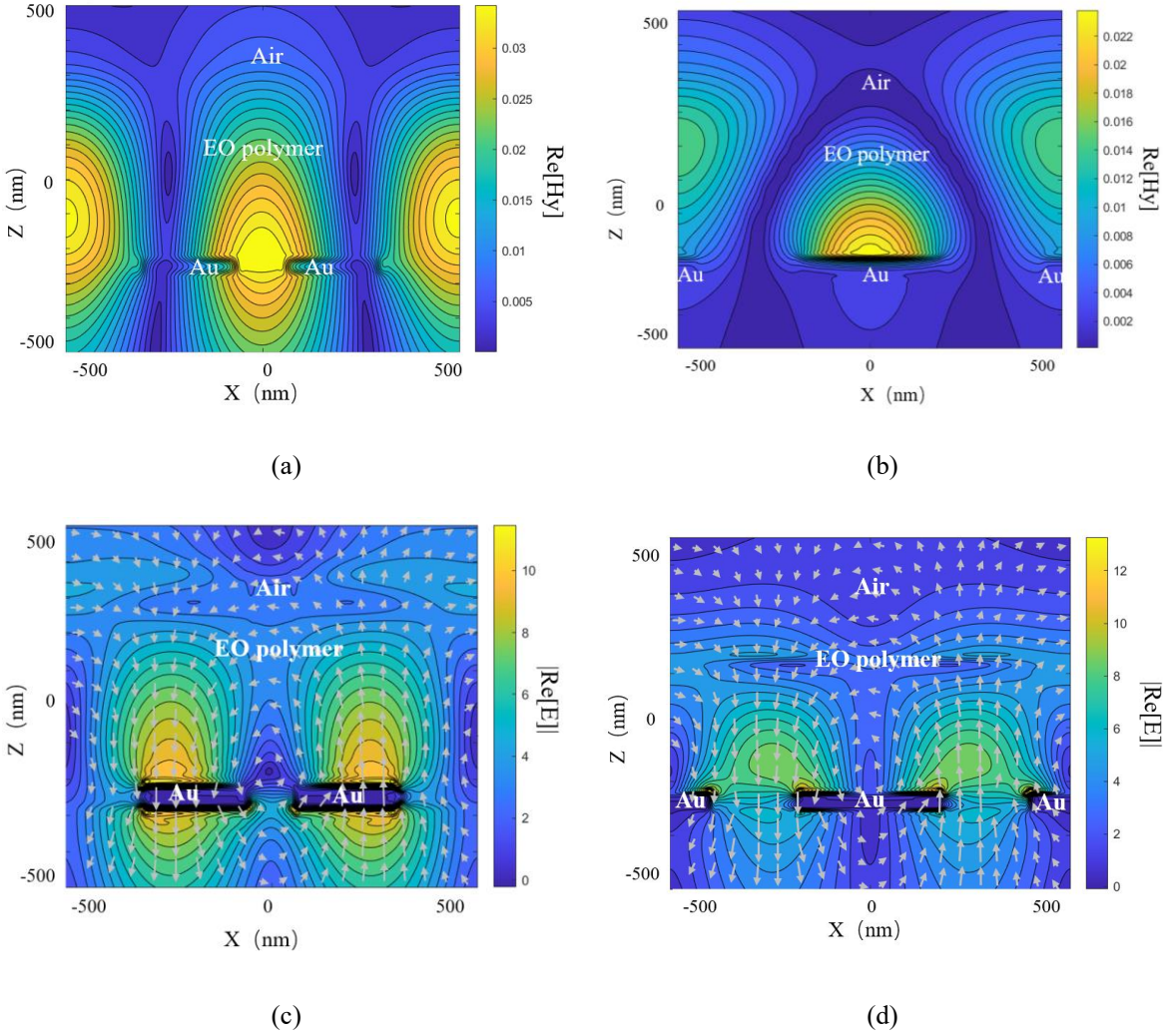

Figure 3.3. Simulated magnetic field profile(H_y) of (a) Gap dimerized grating, (b) Width dimerized grating. Simulated electric field profile($E_{x,z}$) of (c) Gap dimerized grating. (d) Width dimerized grating ((a)Λ=1000nm, FF = s/Λ=0.5 tg=550nm, δ=0.05. (c)Λ=1000nm, FF = s/Λ=0.5 tg=550nm, δ=0.05). The color indicates the amplitude of the field, while the gray arrows indicate the direction of the electric field.)

In the M2 mode coupled by the width-dimerized grating, the electric field is mainly distributed between the electrodes as shown in figure 3.3(d). While in the M1 mode coupled by the gap dimerized grating, the electric field is more concentrated above and below the electrodes as shown in figure 3.3(c). In the following discussion, we focus on gap dimerized structure, because the optical mode distribution in the polymer layer matches the static electric field distribution, which determines the direction and magnitude of r_{33}.

3.2.4 Q value for different perturbation

The total Q factor is the overall quality factor of the system, representing the combined effect of all loss mechanisms, including radiative loss and absorption loss. The higher the total Q factor, the better the quality of the system.

The relationship between the total factor (Q_{tot}), the radiative quality factor (Q_{rad}) and the absorption quality factor (Q_{abs}) is

$$\frac{1}{Q_{tot}} = \frac{1}{Q_{rad}} + \frac{1}{Q_{abs}}$$

When $Q_{rad} = Q_{abs}$, the critical coupling condition is met.

The absorption-related quality factor (Q_{abs}) represents the energy loss due to material absorption. The radiative Q factor represents the energy loss due to radiative dissipation. Since the main loss of the system is radiative loss, Q_{ext} can be directly reflected by Q_{rad}. As mentioned in the principle, by varying the perturbation (δ), the Q_{ext} can be controlled according to the relation $Q_{ext} \propto \frac{1}{\delta_L{}^2}$.

As shown in figure 3.4(a), only changing the perturbation (δ) does not significantly alter the wavelength, but the reflectivity decreases at certain δ values. In the gap dimerized grating, changes in the perturbation (δ) can result in observable variations in reflectivity.

When the perturbation decreases, the supported leaky mode eventually decouples from free-space radiation, forming a bound state, which causes Q_{rad} significant increasing. As perturbation (δ) grows, the field distribution gets distorted and the dissipation on the top surface of the metal strips increases, leading to a decreasing Q_{abs}. Meanwhile, the radiation dissipation increases, reducing Q_{rad}, and thus, Q_{tot} shows a downward trend as shown in figure 3.4(b).

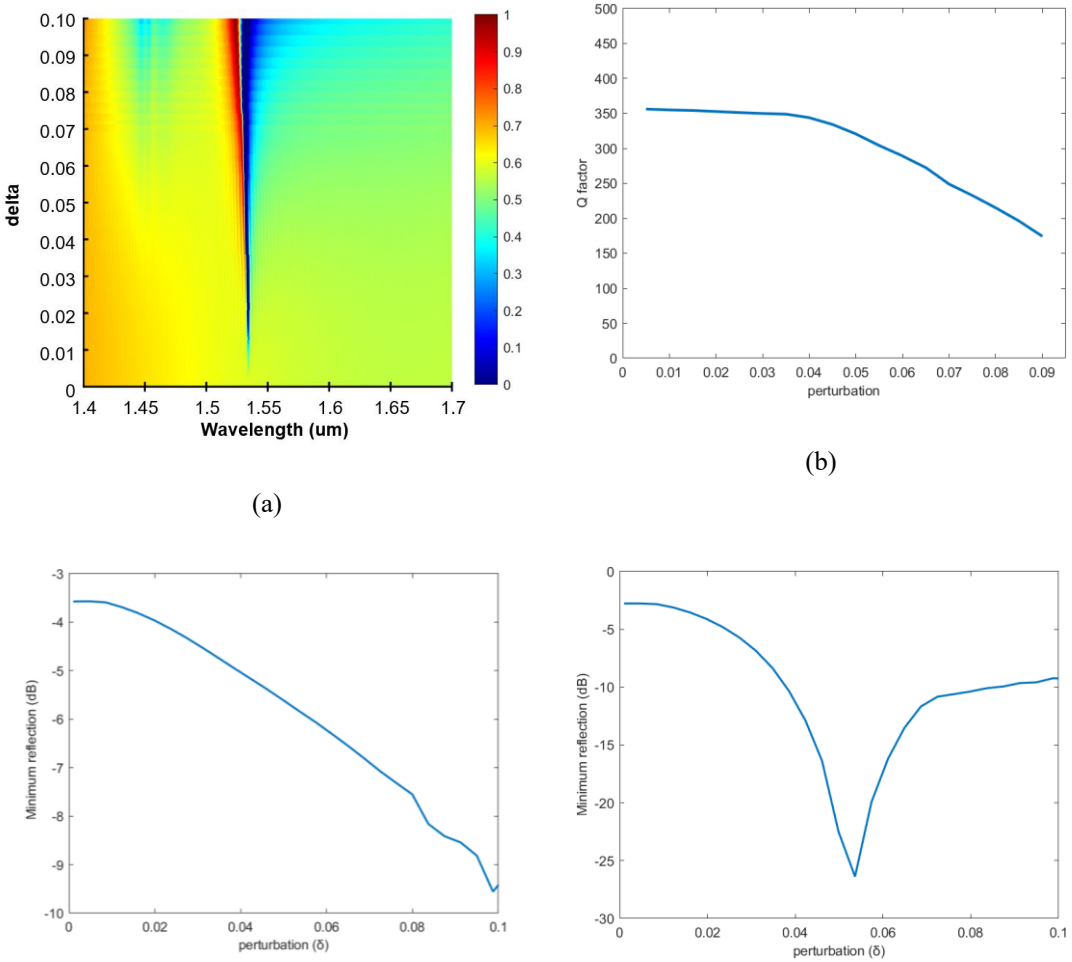

(a) (b)

(c) (d)

Figure. 3.4 (a) Reflection spectrum (period=1000nm, FF = s/Λ=0.5, EO polymer thickness =670nm) (b) Q factor with different perturbation δ. (period=1000nm, FF = s/Λ=0.5, EO polymer thickness=670nm) (c) Minimum reflection with different perturbation δ when EO polymer thickness =550nm. (d) Minimum reflection with different perturbation δ when EO polymer thickness =670nm.

With the EO polymer thickness of 550 nm, regardless of changes in the value of perturbation (δ), the system remains in under coupling, as shown in figure. 3.4(c). By varying EO polymer thickness, we can alter Q_{abs} and achieve critical coupling. When we set the EO polymer thickness to 670 nm, the critical coupling occurring around δ = 0.055, as shown in figure. 3.4(d), where the reflectivity reaches a minimum.

3.2.5 Robustness of proposed structure

During the manufacturing process, we use spin-coater to spin coating the EO polymer. Spin-coating results in an uneven EO polymer thickness and cannot achieve the precise

thickness we desire. Thus, to investigate the robustness to manufacturing errors, we simulated the performance when changing the thickness of the EO polymer. To improve the modulation performance of the modulator, we aim to achieve a stable and higher Q-factor.

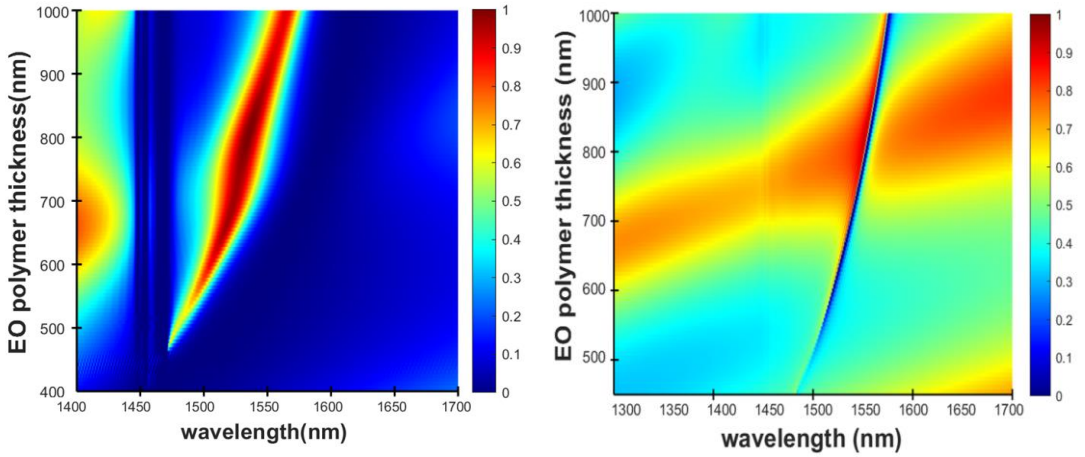

(a) (b)

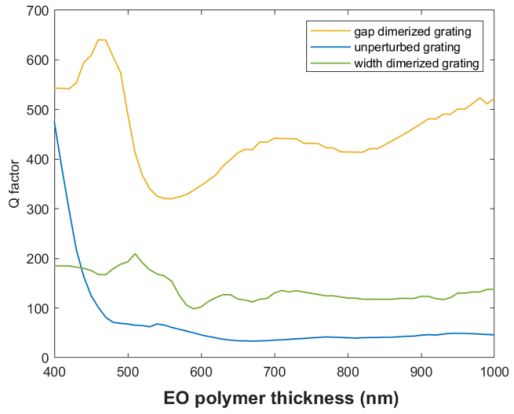

(c)

Figure 3.5. (a) Simulated transmission spectrum of unperturbed dimerized grating with different EO polymer thickness. (b) Simulated transmission spectrum of gap dimerized grating with different EO polymer thickness. (c) Q factor of (a), (b), (c). ((a) Unperturbed grating: period=1800nm, FF = s/Λ=0.5, δ=0. (b) Gap dimerized grating: period=1000nm, FF = s/Λ=0.5, δ=0.05. (c) Gap dimerized grating: period=1000nm, FF = s/Λ=0.5, δ=0.05)

The decrease in film thickness will make the distribution of the optical field more concentrated within the polymer layer. This concentration effect enhances the interaction between light and the material, reducing the loss of light during propagation,

improving the Q factor. However, the decrease in film thickness also causes the optical field to be more concentrated in the high-loss metal regions, increasing plasmonic losses. This type of loss will decrease the radiation quality factor (Q_{rad}), thus reducing the overall Q-factor.

From figure 3.5(c), we can see that both the gap dimerized grating and the width dimerized grating have higher Q factor than the unperturbed grating at EO polymer thickness higher than 450nm. In the gap dimerized grating, the resonance can maintain a high Q factor over a wide EO polymer thickness range. The width dimerized grating has higher Q than the unperturbed grating when EO polymer thicknesses greater than 450 nm. It can be said that both gap dimerized grating and width dimerized grating have better robustness in the electro-optic polymer thickness while exhibiting a higher Q factor.

3.2.6 Modulation efficiency

When an external voltage is applied to the electrodes, the refractive index of the polymer will change due to the Pockels effect.

Figures 3.6(a), (b) and (c) show the changes in the transmission spectrum in dB format under modulation. When Δn changes from -0.01 to 0.01, the wavelength shift is 17.74nm in the unperturbed grating, 13.14nm in the gap dimerized grating and 17.41nm in the width dimerized grating. The Q factor of the unperturbed grating is 65, while that of the gap dimerized grating is 320 and of the width dimerized grating is 165. Compared to the unperturbed grating, the dimerized grating has a higher Q factor due to the introduction of SP BIC. The gap dimerized grating has higher Q factor compared to width dimerized grating because M2 mode has higher losses compared to M1 mode, affects the overall performance. In the gap dimerized grating, only the M1 mode propagates while only M2 mode propagates in width grating. Thus, the resonance mode of the gap dimerized grating is not influenced by M2 mode, resulting in lower losses.

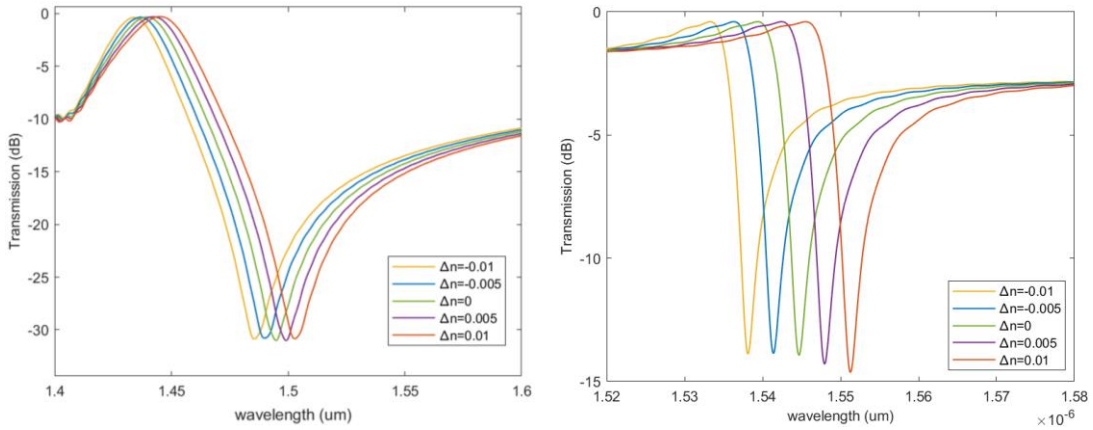

(a) (b)

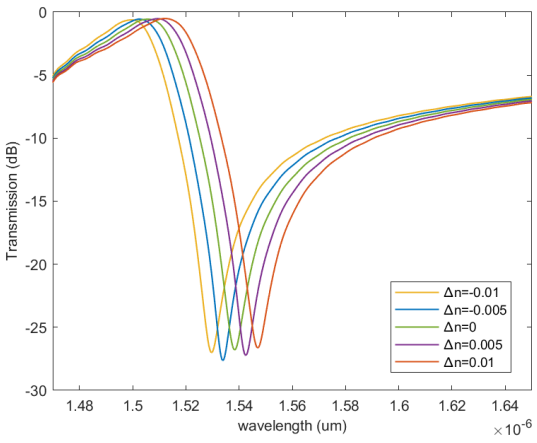

(c)

Figure 3.6 Simulated reflection spectrum shift of (a) Unperturbed grating, (b)Gap dimerized grating and (c)Width dimerized grating ((a) Unperturbed grating: period=1900nm, FF = s/Λ=0.5, EO polymer thickness=550nm, δ=0 (b)Gap dimerized grating: period=1000nm, FF = s/Λ=0.5, EO polymer thickness=670nm, δ=0.07 (c)Width dimerized grating: period=1000nm, FF = s/Λ=0.5, EO polymer thickness=550nm, δ=0.07)

Assuming r_{33} is 200 pm/V, based on the relation $\Delta n = -0.5 n_0^3 r_{33} {}^{V_0}/_{d}$, the required voltage to achieve a change of Δn= ±0.01 in the unperturbed grating is ±10.57V, while that of the gap dimerized grating is ±5.84V and that of the width dimerized grating is ±5.57V. The drive voltage of both dimerized grating is lower than unperturbed grating.

The metal strips forming the grating can be used as complementary electrodes when applying voltage. So, we did simulations for the case where only the refractive index of the polymer between the two electrodes is changed to simulate the measurement

scenario.

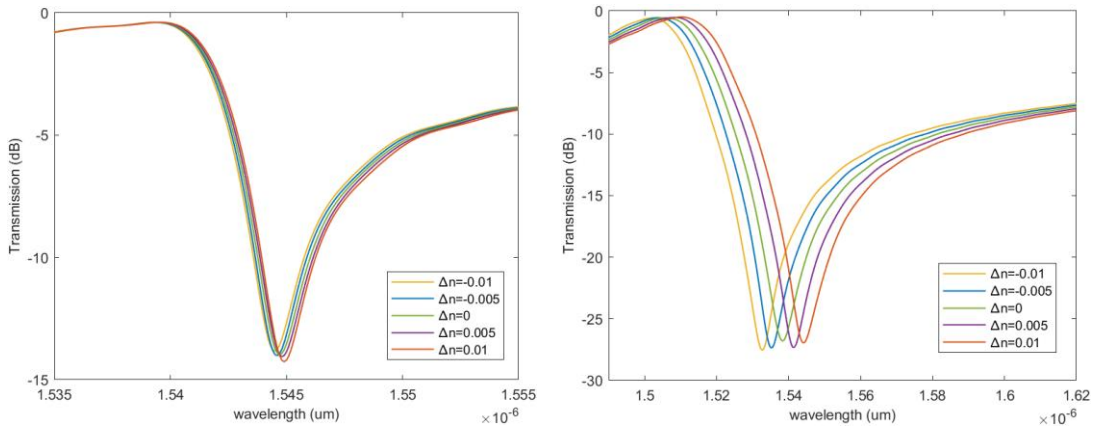

(a) (b)

Figure 3.7 Simulated reflection spectrum shift when the refractive index of the polymer changes between only two grating of (a) Gap dimerized grating and (b)Width dimerized grating

Figure 3.7 shows the case of changing only the refractive index of the polymer between the two electrodes. In the gap dimerized case, the electric field is concentrated mainly on the upper and lower sides of the electrodes as shown in the mode profile, so that the wavelength shift is small, only 0.78 nm. In the width dimerized case, the electric field is mainly concentrated between the electrodes as shown in the mode profile, so the shift of the wavelength is 12.03nm, which is just a little smaller than in the normal case.

3.2.7 Modulation speed

The 3 dB bandwidth is an important measure of response speed, a wider bandwidth usually indicates that the system can respond faster to changes in the input signal. In modulators using EO polymer, the photon lifetime of the resonance and RC constant are the main limiting factors of 3dB bandwidth.

For the factor of photon lifetime τ, it can be calculated by $\tau = \frac{Q\lambda_r}{2\pi c}$. When the Q value is at 200, the photon lifetime is 1.6×10^{-13} s, which also means that the bandwidth of the photon lifetime is about 6.25 THz. Therefore, the photon lifetime will not be the limitation in practical applications, and the main factor limiting the

bandwidth is the RC bandwidth in the devices of this research.

For the RC constant, when focused on the grating structure, the equivalent circuit is shown in Figure 3.8. The equivalent circuit consists mainly of the resistance of Au grating, the resistance between the Au electrodes and the capacitance between the Au electrodes. For actual measurement conditions, other resistance and capacitance should also be considered.

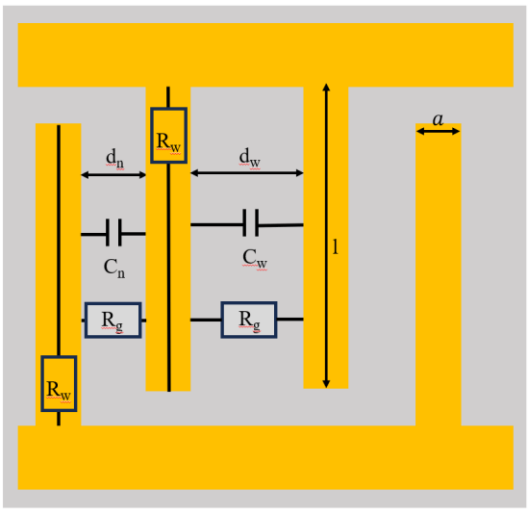

Figure. 3.8 Equivalent circuit of the modulator

The distance between the gold electrodes is very short, and the resistance path is also very short, resulting in a very small resistance between the gold electrodes so that the resistance between the two gratings can be neglected.

The Au grating resistance can be expressed as

$$R_w = \frac{l}{\sigma_{Au} a h}$$

in which a is the width of the Au grating, h is the height of the Au grating, l is the length of the Au grating and σ_{Au} is the conductivity of the Au.

We assume the electric field is mainly concentrated in the EO polymer between the Au electrodes (such as unperturbed grating and width grating), the capacitance between Au electrodes can be approximated as a parallel plate capacitor. So, the capacitance can be expressed as

$$C = \varepsilon_0 \varepsilon_{EO} \frac{lh}{d}$$

in which ε_0 is the vacuum dielectric constant, ε_{EO} is the relative dielectric constant of the EO polymer, l is the Au electrode length, d is the distance between the Au electrodes, and h is the thickness of the gold.

However, the distance between gratings is not the same because perturbations are added. According to the previous definition of the perturbation, if the average grating distance is assumed as d_a, the distances between the gratings can be defined as

$$d_n = d_a - 2\delta l$$

$$d_w = d_a + 2\delta l$$

So, the capacitance between the gold electrodes can be expressed as

$$C_{all} = \frac{1}{2}\left(\varepsilon_0 \varepsilon_{EO} \frac{lh}{d_n} + \varepsilon_0 \varepsilon_{EO} \frac{lh}{d_w}\right) = \frac{lh}{2} \varepsilon_0 \varepsilon_{EO} \left(\frac{1}{d_n} + \frac{1}{d_w}\right)$$

$$= \frac{lh}{2} \varepsilon_0 \varepsilon_{EO} \left(\frac{2d_a}{(d_a - 2\delta l)(d_a + 2\delta l)}\right) \approx \varepsilon_0 \varepsilon_{EO} \frac{lh}{d_a}$$

Therefore, the 3dB bandwidth can be expressed as:

$$f_{3dB} = \frac{1}{2\pi RC} = \frac{\sigma_{Au} a d_a}{2\pi \varepsilon_0 \varepsilon_{EO} l^2}$$

The relationship between the Au electrode length l and 3dB bandwidth is shown in Fig. 3.9. From this figure, the 3dB bandwidth can exceed 100GHz if the grating length is less than 500μm.

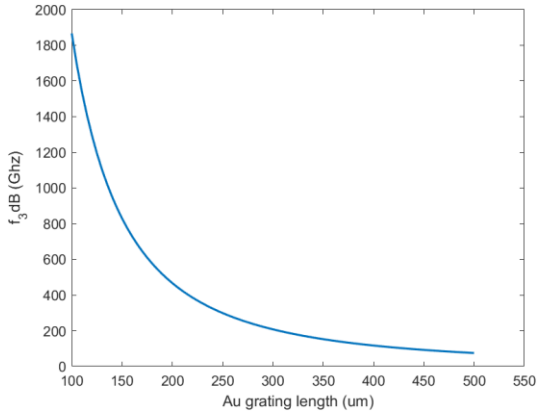

Figure. 3.9 RC bandwidth with different Au grating length l.

3.3 Conclusion

In this chapter, the optical properties of the modulator are simulated by using the FDTD. In this simulation, by introducing perturbation, we achieve an improvement of the Q factor and robustness. Then, based on the assumption that the EO factor r_{33} is equal to 200 pm/V, we show through numerical simulations that 15 dB intensity modulation is achieved at ±5.57 V driving voltage in gap dimerized grating. For width dimerized grating, the intensity modulation is around 25 dB. Also, we calculated the RC constant and photon lifetime of the device. The results show the 3 dB bandwidth greater than 100 GHz.

Chapter 4. Device fabrication and Measurement

4.1 Fabrication process

4.1.1 General fabrication process

The fabrication flow is illustrated in Figure 4.1, and the details of each step will be further described.

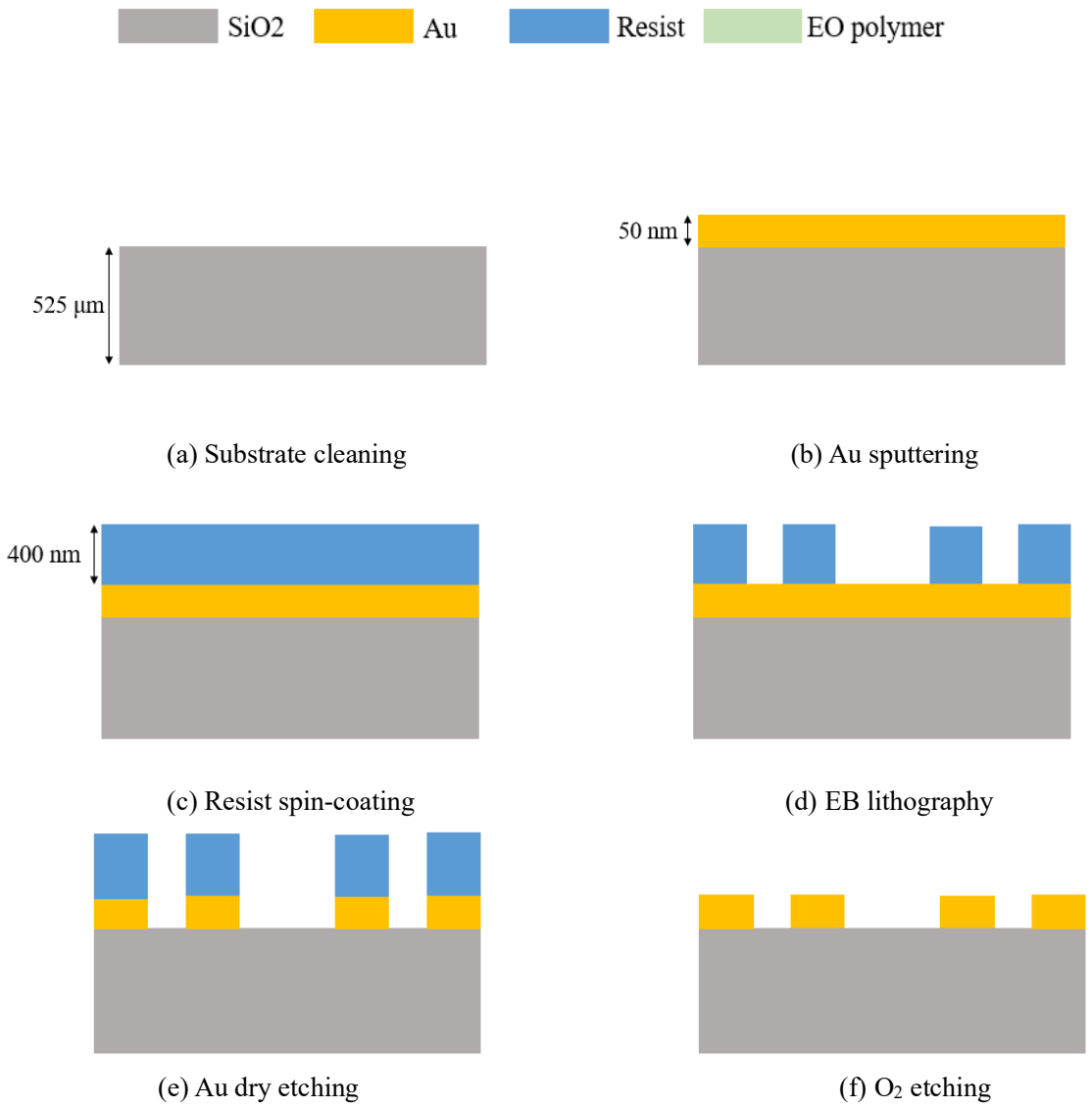

(a) Substrate cleaning

(b) Au sputtering

(c) Resist spin-coating

(d) EB lithography

(e) Au dry etching

(f) O_2 etching

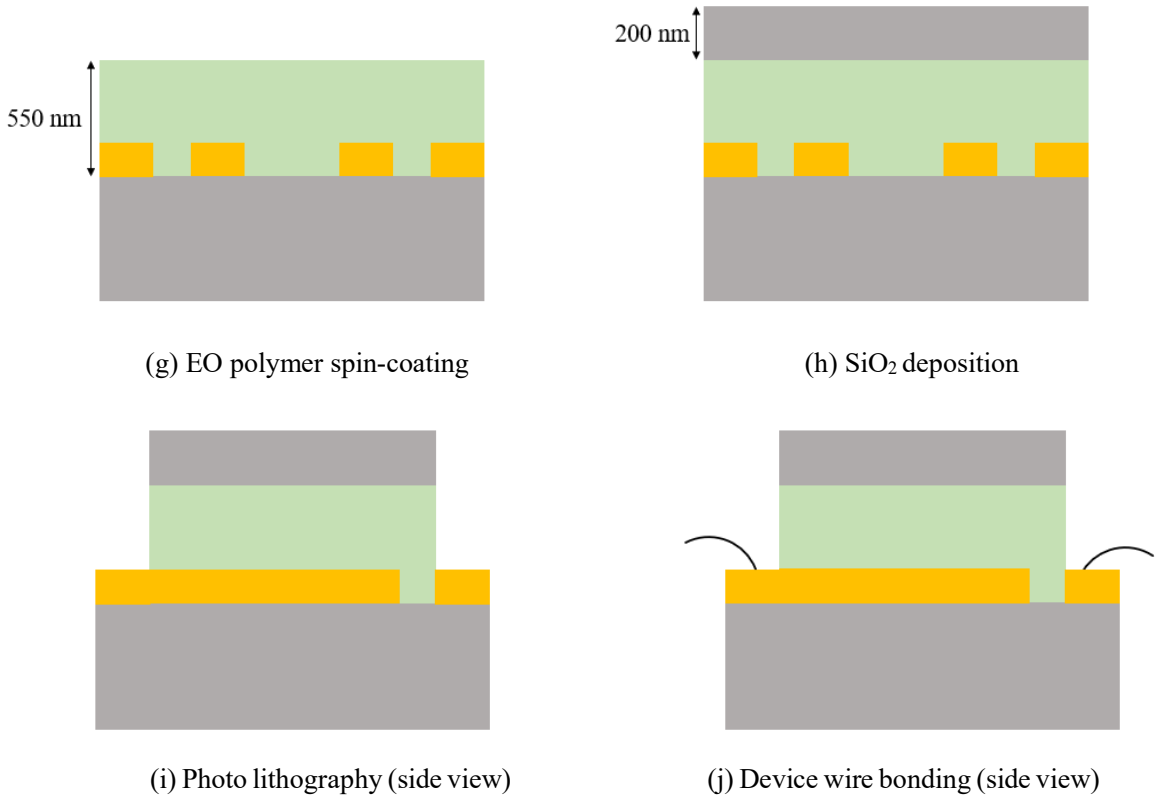

(g) EO polymer spin-coating (h) SiO_2 deposition

(i) Photo lithography (side view) (j) Device wire bonding (side view)

Figure. 4.1 General fabrication flow for the single-layer EO polymer modulator.

(a) Substrate cleaning

In this study, silicon dioxide is selected as the substrate due to its cost-effectiveness. The substrate, which has a square of 3 inch and thickness of 525um, needs to be cut and divided into chips with dimensions of 12mm on each side.

Organic cleaning for the substrate is necessary before proceeding to the subsequent processes. During the organic cleaning process, the chips will be sequentially immersed in acetone, isopropyl alcohol (IPA), and ethanol for 30 seconds each and then subjected to ultrasonic cleaning. Following the cleaning, a nitrogen purge will be conducted, followed by a 10-minute baking process at 120°C to ensure complete evaporation of any remaining liquid from the surface. Subsequently, a surface check will be carried out to ensure the surface is sufficiently clean. If the surface contains large particle impurities, it will have effect on the Au sputtering and EB lithography steps.

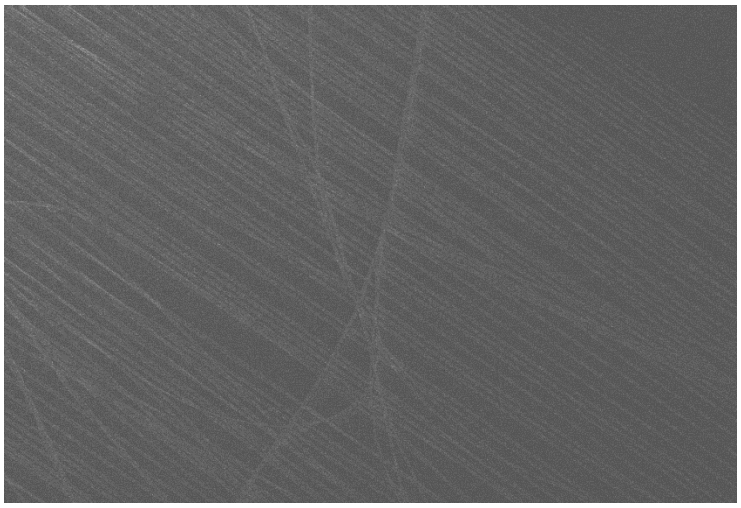

Figure. 4.2 SEM image of damage to metal grating caused by cleaning issues.

(b) Au sputtering

After cleaning the substrate, a 50 nm thick bottom Au layer is directly sputtered onto the silicon dioxide substrate using the SHIBAURA CFS-4EP-LL in the Takeda clean room. In this step, the generation of scratches should be avoided as much as possible to prevent any impact on the EB lithography processes. The sputtering processes for the Au are detailed in Table 4.1.

Target	Ar flow (sccm)	RF power (W)	Temperature (℃)	Rate (nm/sec)	Time (s)
Au	23	200	23	0.383	131

Table. 4.1 The recipe of Au sputtering

(c) Resist spin-coating

In this step, OPA and ZEP520A are typically used as key components of the EB lithography process in the spin-coating process to form the desired pattern structure. The OAP is employed as the primer, and the EB resist ZEP520A is used for EB lithography. Following the spin-coating process, a ZEP520A layer approximately 400 nm thick will be formed on the Au layer. The specific conditions for the resist spin-coating and baking are provided in Table 4.2.

Resist	Upper time (s)	Rotation speed (rpm/min)	Keep time (s)	Baking condition
OAP	5	3000	30	110℃ for 1 min
ZEP520A	5	4000	60	180℃ for 5 min

Table. 4.2 EB resist spin-coating and baking conditions

(d) EB lithography

The EB lithography is performed by using the ADVANTEST F7000S-VD02 EBL machine. The dose factor is set to 104 μC/cm^2 or 105 μC/cm^2. In this step, the GDS pattern will be shown onto the photoresist ZEP520A. Following the EB lithography, the sample is immersed in the ZED-N50 developer for 1 minute and then rinsed in MIBK (Methyl Isobutyl Ketone) in two separate beakers for 5 and 30 seconds, respectively. By using the ZED-N50, contaminants and some oxidized layers on the sample surface can be removed, resulting in high-quality images. The MIBK helps to form a uniform liquid film on the sample surface, which contributes to clear images.

(e) Au dry etching

The Au layer is etched by using the ULVAC ICP-RIE CE-300I in the Takeda clean room. The sample is secured to a dummy wafer using silicon grease. In this step, the GDS pattern will be etched onto the Au layer. Therefore, it is preferable to complete the EB lithography and dry etching on the same day to prevent deformation of the photoresist pattern, which could result in changes to the etched pattern. The specific etching recipe are provided in Table 4.3.

Gas	Flow rate (sccm)	Bias (W)	Antenna (W)	Times (s)
Ar	20	50	300	150

Table. 4.3 Details of Au dry etching process

(f) O_2 etching

After etching the pattern to Au layer, the photoresist ZEP520A is removed by O2

etching using the same equipment as for Au dry etching, retaining the formed gold grating and electrodes. The etching recipe are provided in Table 4.4.

Gas	Flow rate (sccm)	Bias (W)	Antenna (W)	Times (s)
O_2	30	38	500	180

Table. 4.4 Details of O_2 etching process

(g) EO polymer spin-coating

After EB lithography and etching process, the Au layer will show the GDS pattern. Then the EO polymer will be spin-coated on the Au layer.

Firstly, the EO polymer solution with the weight ratio (wt) of 12% needs to be configured. To dissolve the powdered EO polymer into a solution, 0.5wt% F556-Cyclohexanone and cyclohexanone need to be added. To fully dissolve the powder, the solution is stirred for 3 hours at 25℃ using a magnetic stirrer at 700 rpm. After stirring, the solution will be filtered through a syringe with a filter into another bottle and then stored in the freezer. The solution should be used within about two weeks due to the pigments in the electrophoretic polymer coalescing, making it impossible to orient them after film formation, even with polarization. Thus, the spin-coating process should be done as soon as possible after the solution is prepared.

The rotation speed of spin-coating process determines the EO polymer thickness. In order spin-coating the EO polymer around 550nm, the spin-coating conditions for spin-coating are listed in Table 4.5.

Rotation speed (rpm)	Time (s)
4000	30

Table. 4.5 Spin-coating condition for 500 nm thick EO polymer with 12% wt solution.

The step of volatilizing the solvent cyclohexanone is necessary after spin-coating to make less effect on the stable of the EO polymer, so baking step need to be done immediately. Baking is first done in atmosphere to relieve residual stresses in the polymer. Then baking is done in vacuum in order to volatilize cyclohexanone more

fully. The baking conditions are shown in Table 4.6.

	Temperature (°C)	Time(min)
Atmosphere baking	140	120
Vacuum baking	120	60

Table. 4.6 Baking condition for removing the solvent

4.1.2 Easy wire-bonding fabrication process

When depositing silica onto polymers, the high temperature or applied voltages during the deposition of SiO_2 may destabilize the EO polymer, resulting in structural changes or degradation of properties. To mitigate these risks, elongated electrodes are designed to avoid the deposition step. Besides, applying voltage during polarization benefits from longer electrodes for better contact.

The other steps remain unchanged compared to the general process, the step of photolithography of the electro-optic polymer is changed to removing EO polymer which is covered on the Au electrode by using Acetone.

(a) Substrate cleaning

(b) Au sputtering

(c) Resist spin-coating

(d) EB lithography

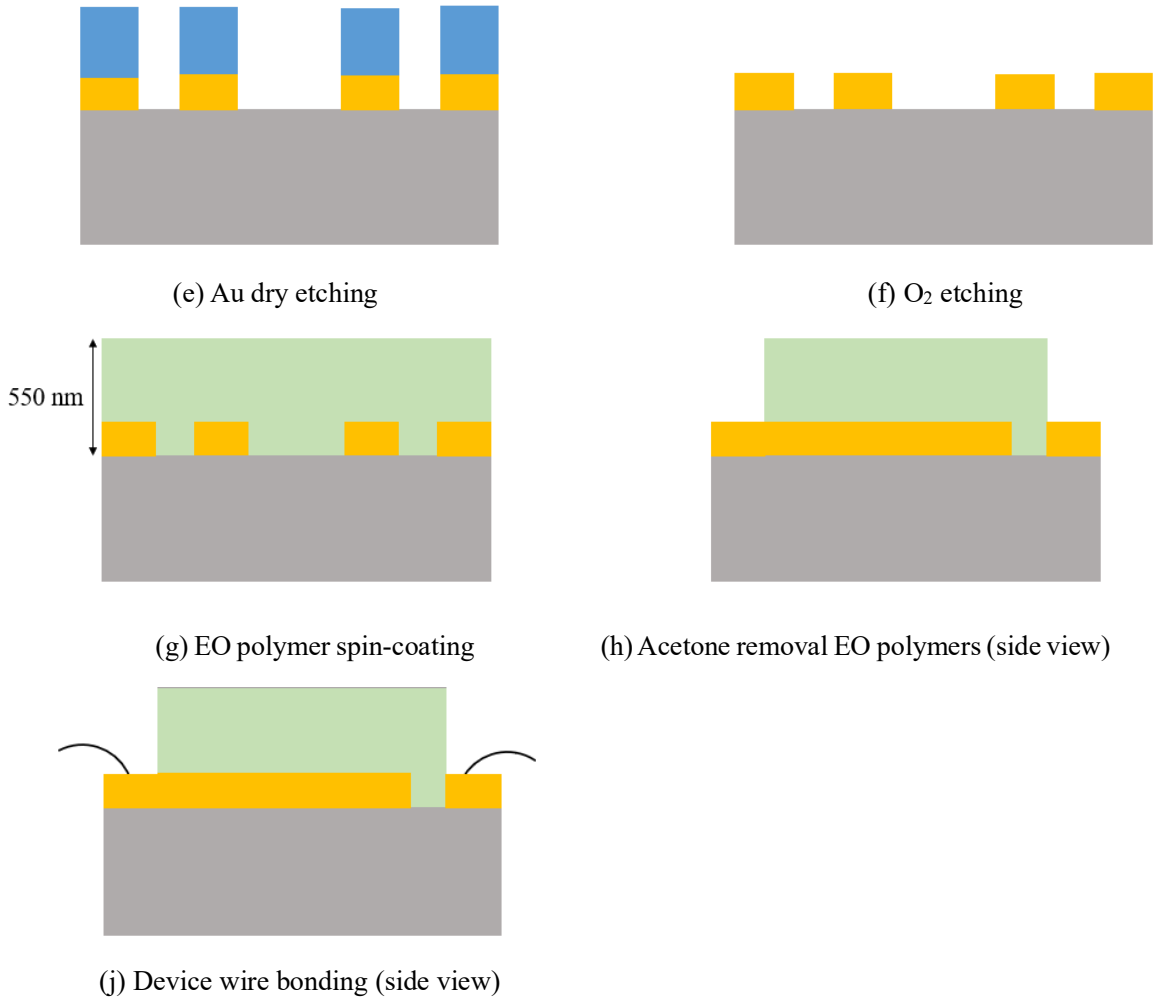

Figure. 4.3 Easy wire-bonding fabrication flow for the single-layer EO polymer modulator.

4.2 Fabricated device

4.2.1 Chip fabricated using general process

We first fabricated the chip using a general process. Based on previous simulations, we determined the unperturbed grating structure to have period of 2200 nm, the Au electrode thickness of 50 nm, the Au electrode width of 550 nm, and the EO polymer layer thickness of around 550 nm. The design GDS pattern is shown in figure 4.4.

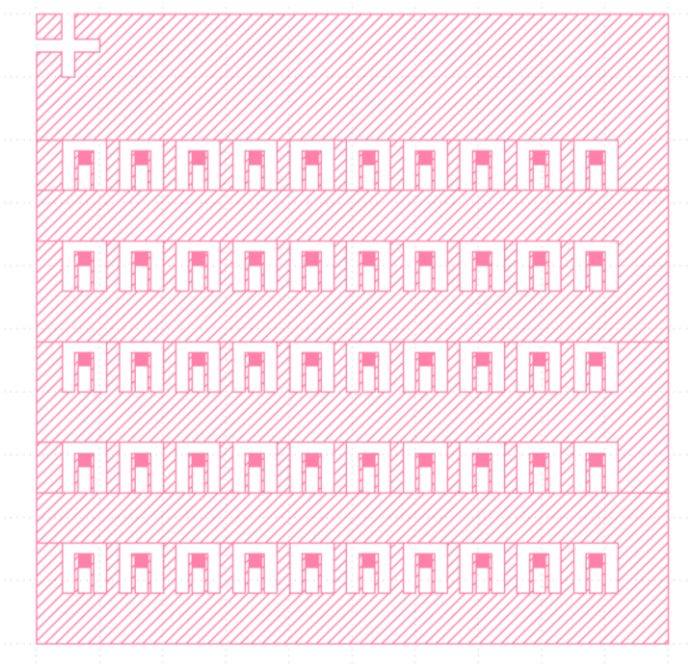

Figure. 4.4 GDS pattern of general process chip.

We performed SEM (Scanning Electron Microscope) after EB lithography to check grating status of the chip. However, unfortunately, the poor adhesion between the SiO_2 and the Au grating resulted in the metal grating peeling off as shown in figure 4.5, making it impossible to proceed with the next step of verification.

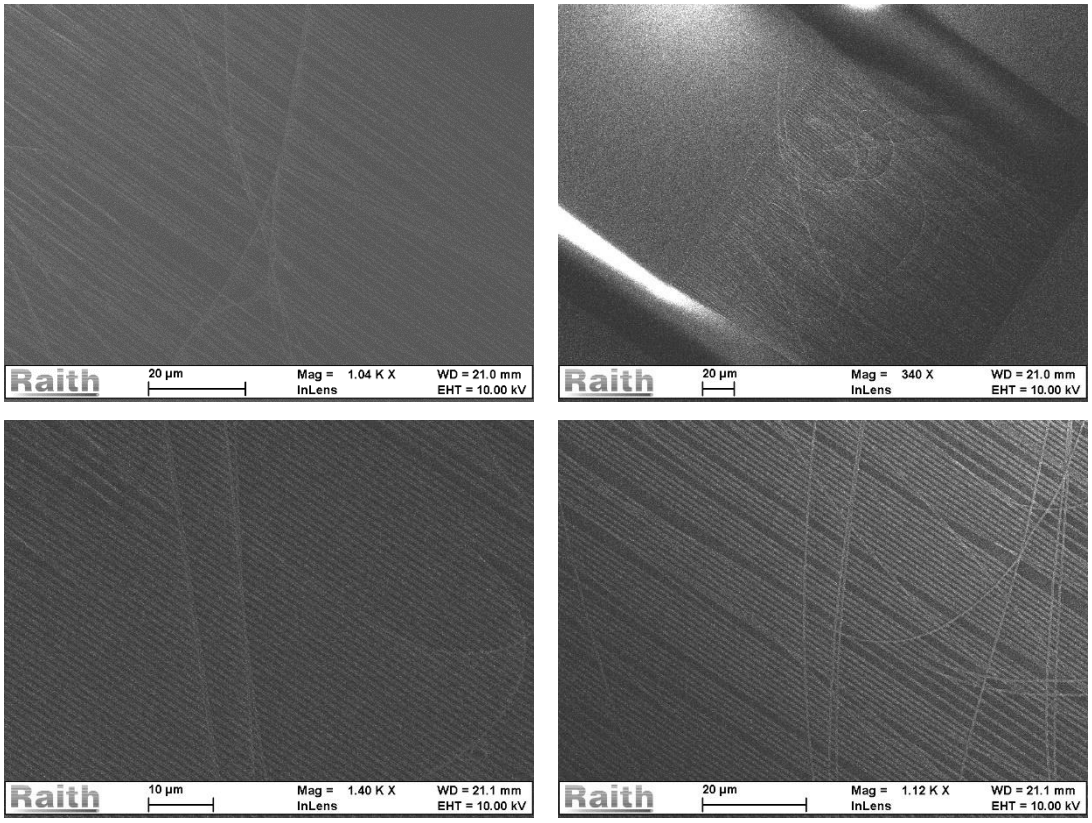

Figure. 4.5 SEM image of mess grating of general process chip.

Then, we created the second version of the GDS pattern of unperturbed grating, shown as figure 4.6. To avoid manufacturing errors affecting the period, we designed two different periods, 2200nm and 2400nm, and aimed to compare the transmittance for the different periods.

This time, we paid extra attention to cleaning and selected an Au-sputtered chip with no scratches in the center. As shown in the SEM image in figure 4.7, we can see that this time the gratings are neatly aligned.

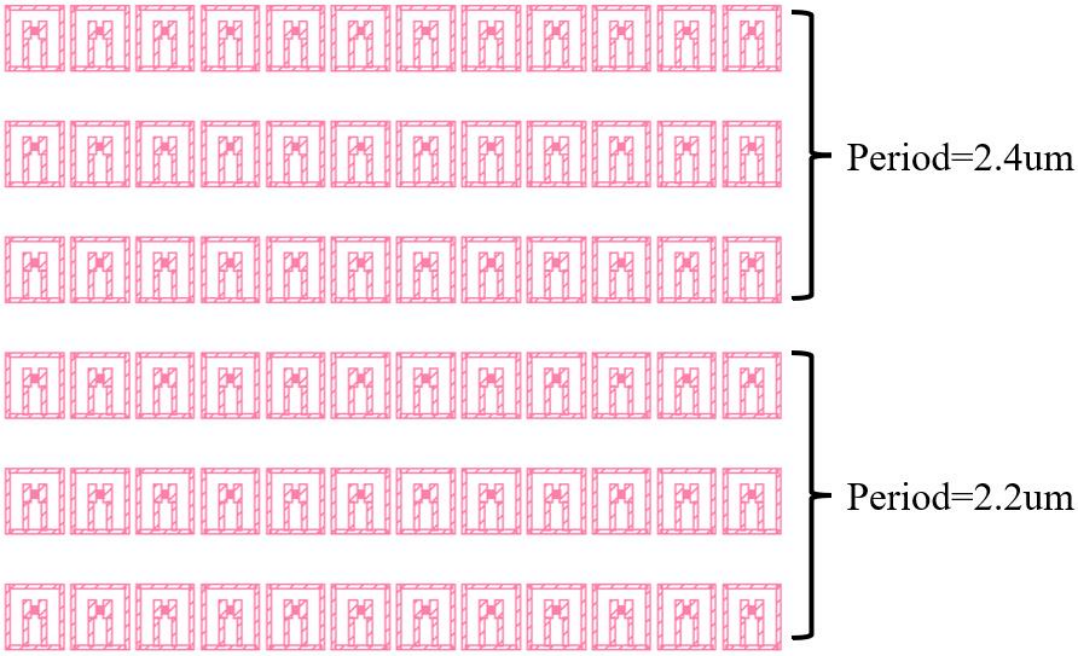

Figure. 4.6 GDS pattern of general process chip with different periods.

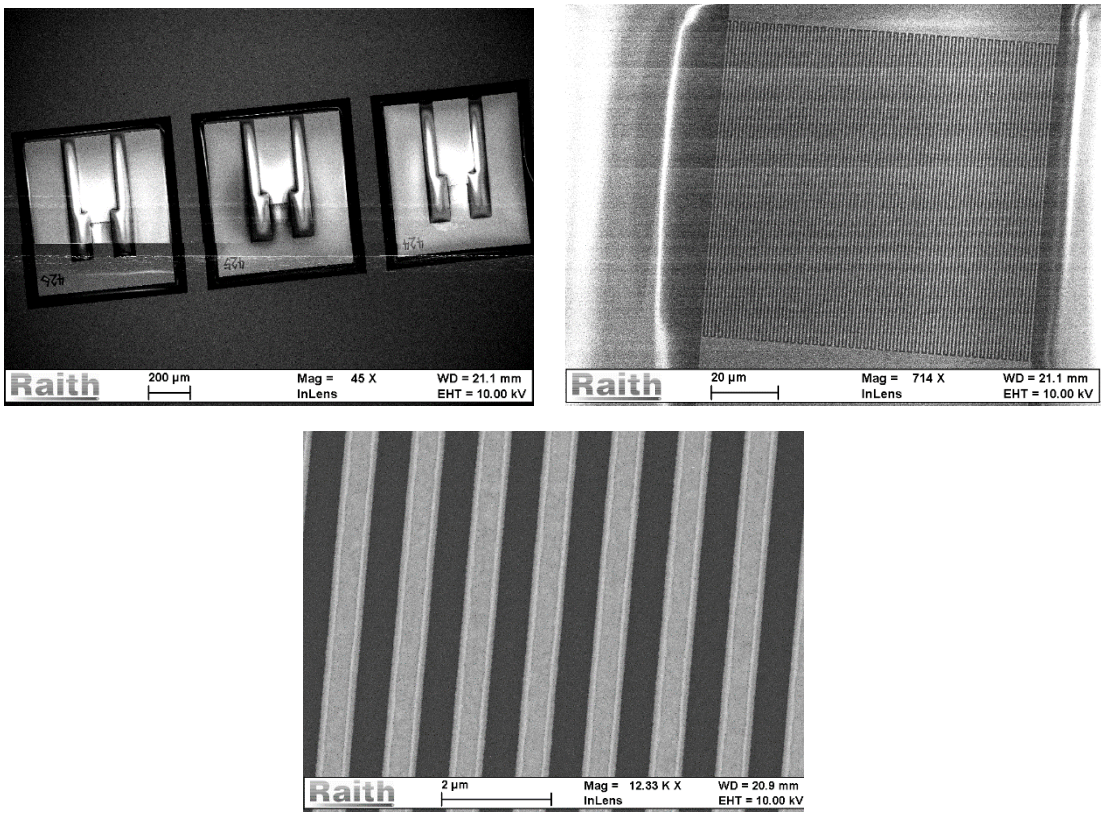

Figure. 4.7 SEM image of neatly grating of general process chip.

Then, we did the EO polymer spin coating on this chip and planned to do the measurement of the reflectivity or transmittance.

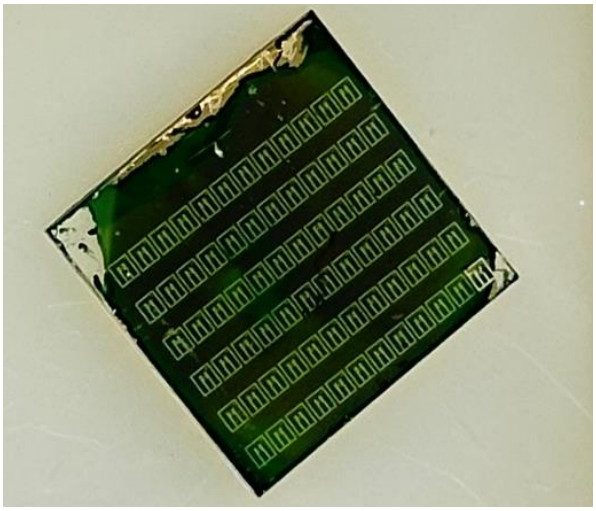

Figure. 4.8 Chip after EO polymer spin-coating and baking.

4.2.2 Chip fabricated using easy wire-bonding process

Considering the impact of silicon dioxide deposition on the EO polymer, we have also designed a structure with extended electrodes. The basic unit structure remains unchanged (the Au grating thickness of 50nm, the EO polymer layer thickness of around 550nm.), but the electrodes have been extended to 1700um to facilitate applying voltage. The GDS pattern of the structure is shown in the figure 4.9.

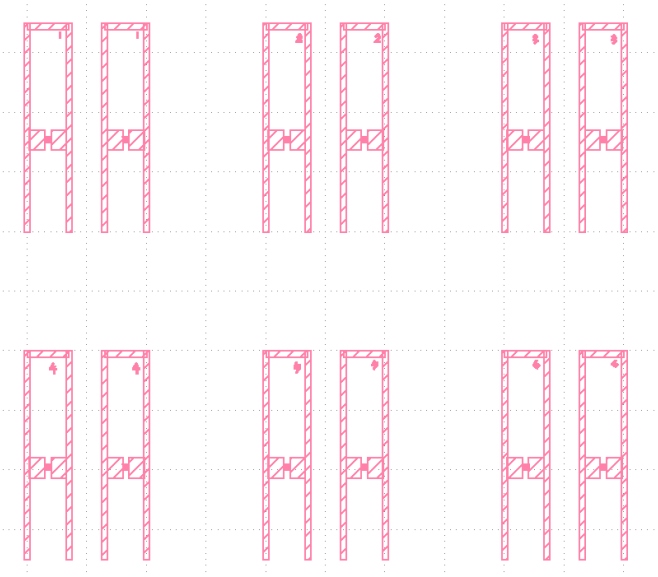

Figure. 4.9 GDS pattern of easy wire bonding structure

Since a larger chip would take more time during EB lithography, we choose the chip size to be 12mm x 12mm. If we select the extended electrodes, we can see that the number of units on the chip will decrease, thereby correspondingly reducing the fabrication fault tolerance rate.

The SEM image is shown in figure 4.10, we can see that some gratings are neatly aligned while others was damaged.

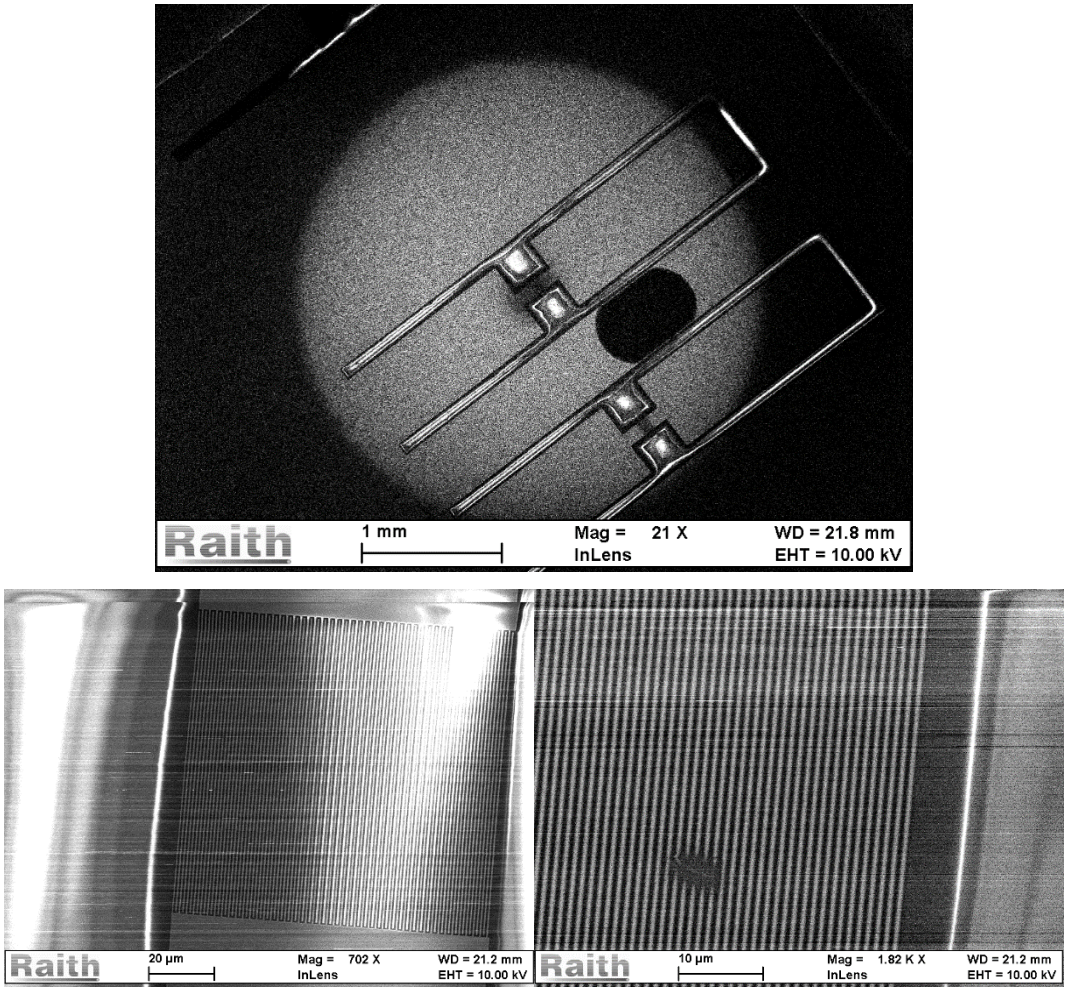

Figure. 4.10 SEM image of neatly grating of general process chip.

Next, we performed spin coating on the chip and used Acetone to remove part of the EO polymer, aiming to expose the electrodes. However, since the Au thickness is only 50 nm and the chip size is small (12nm×12nm) in this experiment, using Acetone to remove EO polymer is easy to destroy the structure.

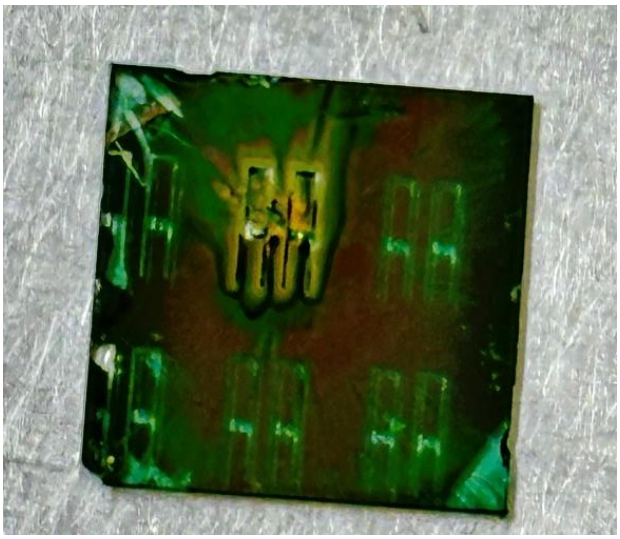

Figure. 4.11 Chip with easy wire bonding structures after EO polymer spin-coating and baking.

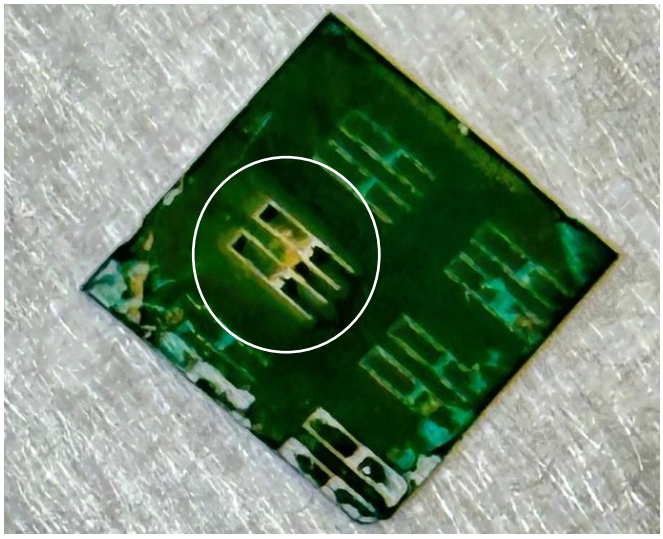

Figure. 4.12 Chip with easy wire bonding structures after Acetone cleaning.

4.3 Measurement

4.3.1 Measurement set up

The schematic figure of reflection spectrum measurement set up is shown in Figures 4.13. This setup is used to measure the reflection spectrum and confirm the reflected light modulation of our fabricated modulators.

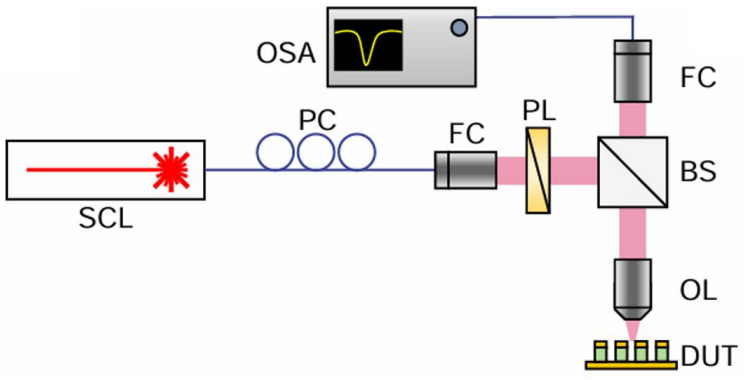

Figure. 4.13. Schematic figure of reflection spectrum measurement set up. (SCL: Super continuum laser, PC: Polarization controller, FC: Fiber collimator, PL: Polarizer, BS: Beam splitter, OL: Objective lens, DUT: Device under test, OSA: Optical spectrum analyzer)

In this set up, the light output from the broadband light source is focused by an objective lens after passing through a polarization controller and then irradiates the device. The reflected light from the device passes through a beam splitter and is coupled into the fiber system, where it is measured by an optical spectrum analyzer. By measuring the reflection spectrum relative to a reference gold mirror, the reflectance spectrum can be obtained.

4.3.2 Measurement of unperturbed grating

We performed passive measurement of the relationship between the reflectivity and the wavelength of the chip. First, we performed reflectivity measurements on the gold-sputtering chip. Then, we measured the reflectivity of our fabricated chip. By comparing the reflectivity, we can obtain the reflectivity of our chip. The reflectivity of different units is shown in Figure 4.14.

Unfortunately, after measuring all the units, the measured reflection spectrum is not matching the simulated reflection spectra., with a maximum dip of only 0.1 dB.

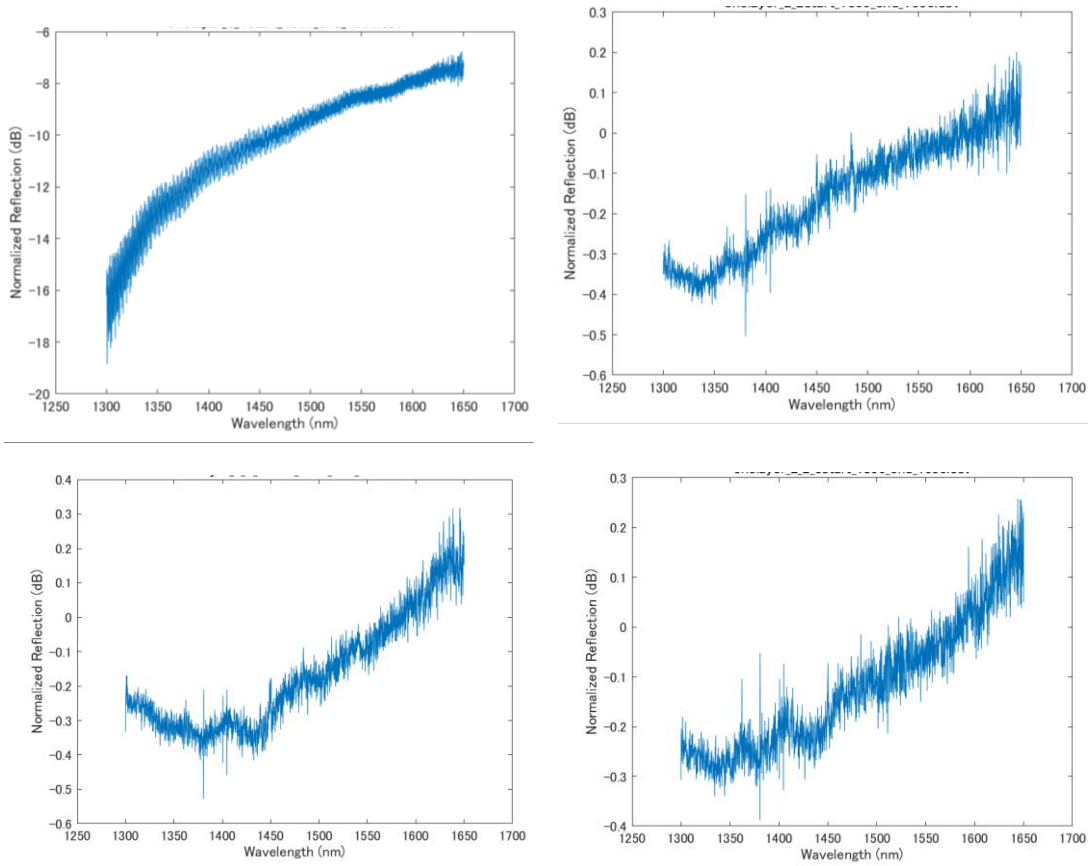

Figure. 4.14. Passive resonance measurement of different units.

Here are the possible reasons we summarized for the no resonance:

1. We use spin-coater to spin-coat the EO polymer layer, resulting in an uneven surface as shown in figure 4.15. This leads to variations in reflection intensity, making it difficult for the signal to accurately reflect the actual situation.
2. During the fabrication process, operations in the EB lithography or etching steps can cause the results in the geometric parameters of the device deviating significantly from the design values, causing a large discrepancy compared to the simulation.

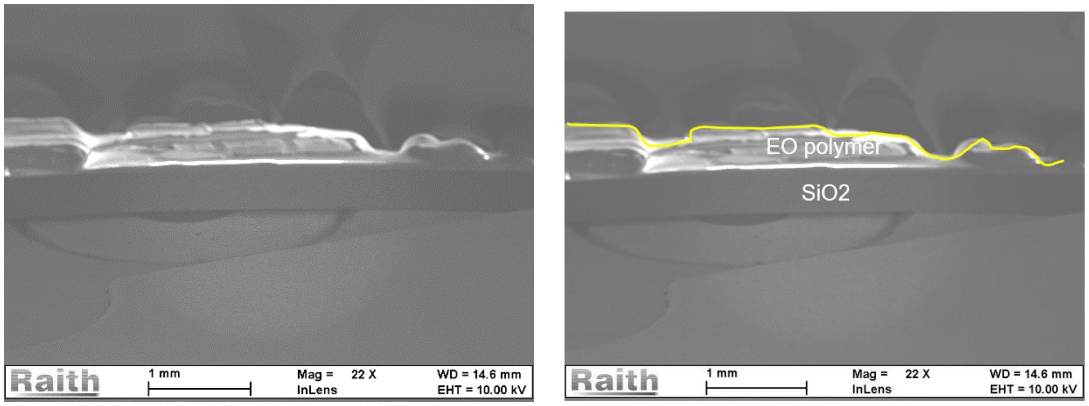

Figure. 4.15. Cross-sectional view of a fabricated chip.

Since the manufacturing process is based on the design of unperturbed grating, we considered how to improve the robustness. Therefore, we introduced perturbation and did the simulations in Chapter 3 to verify its feasibility in terms of robustness.

Chapter 5. Conclusion

In this research, we proposed and designed a surface-normal EO polymer modulator using single layer plasmonic grating, suitable for large-scale two-dimensional array integration. Initially, we simulated and fabricated a modulator with unperturbed grating, but the reflectance dip is not good and does not match the simulation results. Therefore, we introduced the perturbation to improve robustness to fabrication errors while improving modulation speed.

We identified high Q factor resonances of the dimerized plasmonic grating structure through simulation analysis. Assuming an EO polymer r_{33} value of 200 pm/V, utilizing this resonance, we can achieve a 15 dB intensity transmission modulation at around a wavelength of 1550 nm with a modulation voltage of ±5.57 V in gap dimerized grating. For width dimerized grating, the intensity transmission modulation is around 25dB. In designed structures, the Q factor for gap dimerized grating is 320, and for width dimerized grating, it is 165, both of which are greater than those of the unperturbed gratings. We also performed simulations for robustness. The results show that the dimerized gratings have excellent robustness, and regardless of changes in EO polymer thickness, they consistently exhibit high Q-values. Additionally, due to the high conductivity of gold and the low capacitance of the EO polymer, the 3dB bandwidth of this modulator can exceed 100 GHz.

For future work, there are three main issues need to be solved:

1. Improve the adhesion between gold and silica, finding methods to prevent gold from being peeled off.
2. Manufacture chips with single layer dimerized gratings and conduct both active and passive measurements to increase the credibility of the simulation results and demonstrate the device's functionality as an intensity modulator.
3. Integrate the modulator into an array for use in two-dimensional beam control.

Publication

Conference:

1. **Yajing Du**, Koto Ariu, Takuo Tanemura, Yoshiaki Nakano, “Investigation on Electric-Optic Polymer Surface-Normal Modulator using Single-Layer Dimerized Plasmonic Grating”, Technical Committee on OptoElectronics, June. 2023, June 2024.

References

[1] J. Zhang (2019). PhD Thesis, EEIS, The University of Tokyo.

[2] H.Miyano (2023). Master Thesis, EEIS, The University of Tokyo.

[3] Aieta, Francesco, et al. "Aberration-free ultrathin flat lenses and axicons at telecom wavelengths based on plasmonic metasurfaces." Nano letters 12.9 (2012): 4932-4936.

[4] Zheng, Guoxing, et al. "Metasurface holograms reaching 80% efficiency." Nature nanotechnology 10.4 (2015): 308-312.

[5] Zentgraf, Thomas, et al. "Ultranarrow coupling-induced transparency bands in hybrid plasmonic systems." Physical Review B—Condensed Matter and Materials Physics 80.19 (2009): 195415.

[6] Kamali, Seyedeh Mahsa, et al. "Decoupling optical function and geometrical form using conformal flexible dielectric metasurfaces." Nature communications 7.1 (2016): 11618.

[7] Qian, Chao, et al. "Deep-learning-enabled self-adaptive microwave cloak without human intervention." Nature photonics 14.6 (2020): 383-390.

[8] Ju, Yao, et al. "The electro-optic spatial light modulator of lithium niobate metasurface based on plasmonic quasi-bound states in the continuum." Nanoscale 15.34 (2023): 13965-13970.

[9] Benea-Chelmus, Ileana-Cristina, et al. "Electro-optic spatial light modulator from an engineered organic layer." Nature communications 12.1 (2021): 5928.

[10] Sun, Xinyu, et al. "Electro-optic polymer and silicon nitride hybrid spatial light modulators based on a metasurface." Optics Express 29.16 (2021): 25543-25551.

[11] Vinnakota, Raj K., et al. "Plasmonic electro-optic modulator based on degenerate semiconductor interfaces." Nanophotonics 9.5 (2020): 1105-1113.

[12] Hsu C W, Zhen B, Stone A D, et al. Bound states in the continuum[J]. Nature Reviews Materials, 2016, 1(9): 1-13.

[13] Zhong H, He T, Meng Y, et al. Photonic Bound States in the Continuum in Nanostructures[J]. Materials, 2023, 16(22): 7112.

[14] Wang Y, Fan Y, Zhang X, et al. Highly controllable etchless perovskite microlasers based on bound states in the continuum[J]. ACS nano, 2021, 15(4): 7386-7391.

[15] Khattou S, Rezzouk Y, Amrani M, et al. Friedrich-Wintgen bound states in the continuum in a photonic and plasmonic T-shaped cavity: Application to filtering and sensing[J]. Physical Review Applied, 2023, 20(4): 044015.

[16] Gao E, Jin R, Fu Z, et al. Ultrawide dynamic modulation of perfect absorption with a Friedrich–Wintgen BIC[J]. Photonics Research, 2023, 11(3): 456-462.

[17] Koshelev K, Lepeshov S, Liu M, et al. Asymmetric metasurfaces with high-Q resonances governed by bound states in the continuum[J]. Physical review letters, 2018, 121(19): 193903.

[18] Zografopoulos, Dimitrios C., and Odysseas Tsilipakos. "Recent advances in strongly resonant and gradient all-dielectric metasurfaces." Materials Advances 4.1 (2023): 11-34.

[19] Wang, S. S., and R. Magnusson. "Design of waveguide-grating filters with symmetrical line shapes and low sidebands." Optics Letters 19.12 (1994): 919-921.

[20] Hu, Jie, et al. "A review on metasurface: from principle to smart metadevices." Frontiers in Physics 8 (2021): 586087.

[21] Fan, Shanhui, and John D. Joannopoulos. "Analysis of guided resonances in photonic crystal slabs." Physical Review B 65.23 (2002): 235112.

[22] Norton, Scott M., Turan Erdogan, and G. Michael Morris. "Coupled-mode theory of resonant-grating filters." JOSA A 14.3 (1997): 629-639.

[23] Staring E G J. Non-linear optical and electro-optical polymers[J]. Recueil des Travaux Chimiques des Pays-Bas, 1991, 110(12): 492-506.waveguides[J]. Optics letters, 2011, 36(6): 882-884.

[24] Limonov, Mikhail F., et al. "Fano resonances in photonics." Nature photonics 11.9 (2017): 543-554.

[25] Wooten E L, Kissa K M, Yi-Yan A, et al. A review of lithium niobate modulators for fiber-optic communications systems[J]. IEEE Journal of selected topics in Quantum Electronics, 2000, 6(1): 69-82.

[26] Wang S Y, Lin S H. High speed III-V electrooptic waveguide modulators at lambda-1.3 mu m[J]. Journal of lightwave technology, 1988, 6(6): 758-771.

[27] Dalton L, Harper A, Ren A, et al. Polymeric electro-optic modulators: From chromophore design to integration with semiconductor very large-scale integration electronics

and silica fiber optics[J]. Industrial & engineering chemistry research, 1999, 38(1): 8-33.

[28] Wang X, Lin C Y, Chakravarty S, et al. Effective in-device r 33 of 735 pm/V on electro-optic polymer infiltrated silicon photonic crystal slot waveguides[J]. Optics letters, 2011, 36(6): 882-884.

[29] Suh W, Wang Z, Fan S. Temporal coupled-mode theory and the presence of non-orthogonal modes in lossless multimode cavities[J]. IEEE Journal of Quantum Electronics, 2004, 40(10): 1511-1518.

[30] Magnusson R, Wang S S. New principle for optical filters[J]. Applied physics letters, 1992, 61(9): 1022-1024.

[31] Fan S, Joannopoulos J D. Analysis of guided resonances in photonic crystal slabs[J]. Physical Review B, 2002, 65(23): 235112.

[32] Wang S S, Magnusson R. Theory and applications of guided-mode resonance filters[J]. Applied optics, 1993, 32(14): 2606-2613.

[33] Johnson, Steven G., et al. Guided modes in photonic crystal slabs. Physical Review B 60.8 (1999): 5751.

[34] Guo, Tingbiao, et al. "Guided mode resonance in a low-index waveguide layer." Applied Sciences 11.8 (2021): 3312.

[35] Li, Zhuang, et al. "Quasibound states in a one-dimensional grating for electro-optic modulation." Physical Review B 106.12 (2022): 125101.

[36] Magnusson, Robert, and S. S. Wang. "New principle for optical filters." Applied physics letters 61.9 (1992): 1022-1024.

[37] Tamir, Theodor, and Shuzhang Zhang. "Resonant scattering by multilayered dielectric gratings." JOSA A 14.7 (1997): 1607-1616.

[38] Wang, S. S., and R. J. A. O. Magnusson. "Theory and applications of guided-mode resonance filters." Applied optics 32.14 (1993): 2606-2613.

[39] Bukhari, Syed S., J. Vardaxoglou, and William Whittow. "A metasurfaces review: Definitions and applications." Applied Sciences 9.13 (2019): 2727.

[40] Wang, Yuhan, et al. "Highly controllable etchless perovskite microlasers based on bound states in the continuum." ACS nano 15.4 (2021): 7386-7391.

[41] Azzam, Shaimaa I., et al. "Formation of bound states in the continuum in hybrid plasmonic-photonic systems." Physical review letters 121.25 (2018): 253901.

[42] Huang, Jianfeng, et al. "Bound states in the continuum on perfect conducting reflection gratings." Chinese Physics B 30.8 (2021): 084211.

[43] Liu, Jialei, et al. "Recent advances in polymer electro-optic modulators." Rsc Advances 5.21 (2015): 15784-15794.

[44] Dalton, Larry R., Philip A. Sullivan, and Denise H. Bale. "Electric field poled organic electro-optic materials: state of the art and future prospects." Chemical reviews 110.1 (2010): 25-55.

[45] Ullah, Fateh, Niping Deng, and Feng Qiu. "Recent progress in electro-optic polymer for ultra-fast communication." PhotoniX 2 (2021): 1-18.

[46] Qiu, Feng, and Shiyoshi Yokoyama. "Efficiently poled electro-optic polymer modulators." Optics express 24.17 (2016): 19020-19025.

[47] Taghavi, Iman, et al. "Polymer modulators in silicon photonics: review and projections." Nanophotonics 11.17 (2022): 3855-3871.

[48] Teng, Chia-Chi. "High-speed electro-optic modulators from nonlinear optical polymers." Nonlinear optics of organic molecules and polymers. CRC Press, 2020. 441-464.

[49] Günter, Peter, ed. Nonlinear optical effects and materials. Vol. 72. Springer, 2012.

[50] Liu, Jialei, et al. "Progress in the enhancement of electro-optic coefficients and orientation stability for organic second-order nonlinear optical materials." Dyes and Pigments 181 (2020): 108509.

[51] Ayata, Masafumi, et al. "High-speed plasmonic modulator in a single metal layer." Science 358.6363 (2017): 630-632.

[52] Sinatkas, Georgios, et al. "Electro-optic modulation in integrated photonics." Journal of Applied Physics 130.1 (2021).

Acknowledgments

During my time at the University of Tokyo, many people have given me tremendous support and help. Without their support and encouragement, I would not have been able to complete this research. I would like to express my deepest gratitude to everyone who has supported and helped me throughout the completion of this thesis.

First and foremost, I would like to express my gratitude to my supervisor, Prof. Yoshiaki Nakano. He consistently provided profound insights and suggestions during discussions, meetings, and preliminary defense. His optimistic and cheerful spirit has always inspired me to keep going.

Then, I extend my heartfelt thanks to Prof. Takuo Tanemura, for his endless guidance and support throughout my research. His vast knowledge and patient instruction have been instrumental in my academic progress.

Sincere thanks to the members of our lab, technical stuff Mr. Eisaku Kato and students of our lab: Go Soma, Koto Ariu, Chun Ren, Mengyuan Jiang, Keita Hirashima, Seidai Karakida and others if forgot to list, helped me a lot as well both in the research and life.

Special thanks to Koto Ariu for his collaborative spirit and professional expertise. His valuable assistance in experimental design and simulations has been indispensable. I would like to extend my sincere thanks to Mengyuan Jiang for her support. Without her support, I wouldn't have been able to carry on.

A special thanks goes to my family and friends for their unconditional support and understanding during my research period. Their encouragement and love have been a source of confidence for me in facing challenges.

Once again, my heartfelt thanks to everyone who has supported and helped me.

Yajing Du

The University of Tokyo

July 2024